BSGF - Earth Sciences Bulletin 2024, 195, 25
© J. Aubineau *et al.*, Published by EDP Sciences 2024
https://doi.org/10.1051/bsgf/2024025

BSGF
Earth Sciences Bulletin
Available online at:
www.bsgf.fr

Open Access

Magnetic susceptibility controlled by climate-driven weathering intensity

Jérémie Aubineau[1,2,*,a], Paul Y.J. Antonio[2,3,a], Radouan El Bamiki[4], Fleurice Parat[2], Pierre Camps[2], Otmane Raji[4], Es-Said Jourani[4], Jean-Louis Bodinier[4], Mélina Macouin[1], Stuart Gilder[5], Sonia Rousse[1] and Michel Séranne[2]

[1] Géosciences Environnement Toulouse, CNRS UMR 5563 (CNRS/UPS/IRD/CNES), Université de Toulouse, Observatoire Midi-Pyrénées, Toulouse, France
[2] Géosciences Montpellier, Université de Montpellier, CNRS UMR 5243, Montpellier, France
[3] Centre for Planetary Habitability (PHAB), University of Oslo, Oslo, Norway
[4] Geology and Sustainable Mining Institute, Mohammed VI Polytechnic University, Ben Guerir 43150, Morocco
[5] Department of Earth and Environmental Sciences, Ludwig Maximilians University, Munich, Germany

Received: 14 February 2024 / Accepted: 21 October 2024 / Publishing online: 20 December 2024

Abstract – Magnetic susceptibility (MS) variations are commonly attributed to eustatic and/or climatic changes that impact the delivery of fine-grained detrital magnetic minerals. However, the mechanism responsible for sourcing magnetic minerals from land to the ocean is not fully understood. Bulk mineralogy, Rietveld refinements of powder XRD patterns, and whole-rock geochemistry, combined with a MS investigation across a ~290 m-thick Upper Cretaceous/Paleogene sedimentary sequence at Erguita, Morocco, imply that iron is exclusively detrital in origin. Moreover, MS fluctuations occurred independently from depositional setting and sea-level variations. Rock magnetism investigations further show that a complex assemblage of ferromagnetic *sensu lato* minerals is recorded in the Erguita sedimentary section, and a proportion of more or less oxidized magnetite supplied to the depositional setting controls the MS variations. This study chronicles that the weathering of the Anti-Atlas crystalline basement led to the supply of detrital Fe-bearing phyllosilicates and ferromagnetic (*sensu lato*) Fe-oxides to the eastern passive margin of the Atlantic Ocean from the Late Cretaceous to the mid-Paleogene. Higher weathering intensity drove up the detrital magnetic material in all lithologies, which, in turn, increased the MS signal. Importantly, this model nicely coincides with the climatic upheavals of the Paleogene. We propose that this unrecognized link between MS and climate-driven weathering intensity is paramount to unraveling the origin of the low MS interval below the Cretaceous-Paleogene boundary. Climate cooling resulting in reduced weathering rather than a global acidification triggered by Phase 2 of Deccan volcanism could help explain the MS trend at that time.

Keywords: Magnetic susceptibility / weathering / climate / Cretaceous / Paleogene / Erguita / Morocco

Résumé – La susceptibilité magnétique contrôlée par l'intensité de l'altération climatique. Les variations de la susceptibilité magnétique (SM) sont généralement attribuées à des changements eustatiques et/ou climatiques qui ont un impact sur l'apport des minéraux magnétiques détritiques. Cependant, le mécanisme responsable de l'apport de minéraux magnétiques du continent vers l'océan n'est pas entièrement compris. La minéralogie de roche totale, la méthode de Rietveld à partir de diffractogrammes de poudres et la géochimie de roche totale, combinés à une étude de SM sur une séquence sédimentaire du Crétacé supérieur/Paléogène d'une épaisseur de ~290 m à Erguita, au Maroc, impliquent que le fer a une origine exclusivement détritique. Les fluctuations de la SM se sont produites indépendamment du cadre environnemental de dépôt et des variations du niveau de la mer. Les études sur le magnétisme des roches montrent qu'un assemblage complexe de minéraux ferromagnétiques *sensu lato* est enregistré dans la section sédimentaire d'Erguita, et que de la magnétite plus ou moins oxydée contrôle les variations de susceptibilité magnétique Cette étude montre que l'altération probablement du socle cristallin de l'Anti-Atlas

* e-mail: jeremie.aubineau@get.omp.eu
[a] J. Aubineau and P.Y.J. Antonio contributed equally.

This is an Open Access article distributed under the terms of the Creative Commons Attribution License (https://creativecommons.org/licenses/by/4.0), which permits unrestricted use, distribution, and reproduction in any medium, provided the original work is properly cited.

a entraîné l'apport de phyllosilicates détritiques contenant du fer et d'oxydes de fer ferromagnétiques (*sensu lato*) vers la marge passive orientale de l'océan Atlantique, de la fin du Crétacé jusqu'au milieu du Paléogène. L'intensité accrue de l'altération a entraîné une augmentation du matériel magnétique détritique dans toutes les lithologies, ce qui, à son tour, a augmenté le signal de SM. Il est important de noter que ce modèle coïncide parfaitement avec les bouleversements climatiques du Paléogène. Nous proposons que ce lien méconnu entre la SM et l'intensité de l'altération induite par le climat soit primordial pour élucider l'origine de l'intervalle à faibles valeurs de SM sous la limite Crétacé-Paléogène. Un refroidissement climatique entraînant une réduction de l'altération plutôt qu'une acidification globale déclenchée par la phase 2 du volcanisme du Deccan pourrait contribuer à expliquer la tendance à la SM à cette époque.

Mots clés : Susceptibilité magnétique / altération / climat / Crétacé / Paléogène / Erguita / Maroc

1 Introduction

The magnetic susceptibility (MS) has been recently invoked as a proxy to identify the Cretaceous-Paleogene (K-Pg) transition (*e.g.*, Abrajevitch *et al.*, 2015; Font *et al.*, 2011; Lowrie *et al.*, 1990). In principle, better constraints on the relationships between MS and climatic and environmental changes could improve our understanding of the external factors controlling the MS record.

MS, which quantifies the capacity of a material to be magnetized in the presence of a magnetic field, first allows assessing the proportion of detrital-dominated ferromagnetic *sensu lato* (iron oxides), paramagnetic (*e.g.*, Fe-bearing silicates and most of the iron sulfides), and diamagnetic (*e.g.*, iron-free carbonates and quartz) minerals in a given sediment (Ellwood *et al.*, 2000; Riquier *et al.*, 2010). The mineralogical nature of Fe-oxides strongly impacts the MS values (Da Silva *et al.*, 2015). Although paramagnetic and diamagnetic minerals show very low positive or negative MS values, respectively (Ellwood *et al.*, 2000), variations in MS, together with detailed rock magnetic analyses, have been linked to changes in ferromagnetic contribution (Pas *et al.*, 2019; Riquier *et al.*, 2010). Moreover, magnetic minerals with a high coercivity such as hematite yield lower MS signals compared to magnetite, a low coercivity mineral (Da Silva *et al.*, 2013). In sedimentary environments, the primary MS signal is linked to detrital minerals and can be altered by the formation of secondary minerals during diagenesis and metamorphism alteration (Ellwood *et al.*, 2000). Thus, post-depositional processes must be screened for potential modification of the primary MS signature.

MS has been increasingly used to assess the amount of detrital inputs in conjunction with sea level changes, leading to the idea that MS could constitute an independent proxy to document several millions of years of long-term trends of eustatic changes (Da Silva *et al.*, 2015, 2010, 2009; Hladil, 2002; Mahboubi *et al.*, 2019). High MS values were hypothesized to reflect an increasing detrital supply related to sea level fall, particularly in the Frasnian-Famennian transition, where major extinctions coincided with profound eustatic fluctuations (Averbuch *et al.*, 2005; Girard *et al.*, 2021; Riquier *et al.*, 2010). It was supported that MS and sea-level change only covary for a short period of thousands of years (Boulila *et al.*, 2010; Whalen and Day, 2010). Yet, it remains unclear how depositional environments (proximal versus distal) at a given stratigraphic level influenced the MS record.

Several studies have proposed that MS is a correlation tool and generally records paleoclimatic variations (influencing or not eustacy) in sedimentary rocks (Boulila *et al.*, 2010, 2008; Da Silva *et al.*, 2015; Ellwood *et al.*, 2000; Font *et al.*, 2011; Mead *et al.*, 1986; Nowaczyk *et al.*, 2002; Pas *et al.*, 2019; Stage, 2001; Vanderaveroet *et al.*, 1999; Whalen and Day, 2010; Wouters *et al.*, 2019). This inference comes from the relationship between MS trends and oxygen isotopes in Pleistocene sections (Robinson, 1986) and astronomically-driven Milankovitch cycles in Devonian and Jurassic sequences (Boulila *et al.*, 2010; Da Silva *et al.*, 2020, 2015; Ellwood *et al.*, 2015). However, the mechanism that leads to the covariation between climatic variations and MS remains poorly understood.

Here, we explore the MS signal of a ~290 m-thick Upper Cretaceous/Paleogene phosphorus (P)-bearing sedimentary sequence at Erguita in the Moroccan western High Atlas (WHA), where the sequence stratigraphic framework is well-established (El Bamiki *et al.*, 2020). We use a combination of mineralogical, rock magnetism, and geochemical techniques to demonstrate the detrital origin of MS signal across the section. Then, we provide evidence linking MS variations to climate-driven weathering intensity. The findings also offer new insights on using MS records in deep geological time.

2 Geological background

2.1 General information

The ENE-trending High Atlas Mountain belt in Morocco belongs to the Atlas system that spreads over thousands of kilometers from the Atlantic coast to Tunisia. The tectonic convergence between the African and Eurasian plates since the Late Cretaceous has promoted the inversion of the Mesozoic-Cenozoic intracontinental basin (Atlasic basin) during which former syn-rift faults were reactivated (Frizon de Lamotte *et al.*, 2008; Michard *et al.*, 2008).

The Triassic Central Atlantic rifting initiated the formation of the Atlasic basin in Morocco, which resulted in important thermal subsidence and subsequent deposition of km-thick Mesozoic marine sequences near the rifted zones (Ellouz *et al.*, 2003). This is in contrast to the thin Upper Cretaceous-Paleogene sedimentary successions that were formed when thermally-induced subsidence stopped at the initiation of the Africa-Eurasia convergence (Ellouz *et al.*, 2003). In Morocco, a tremendous amount of phosphate-rich sediments

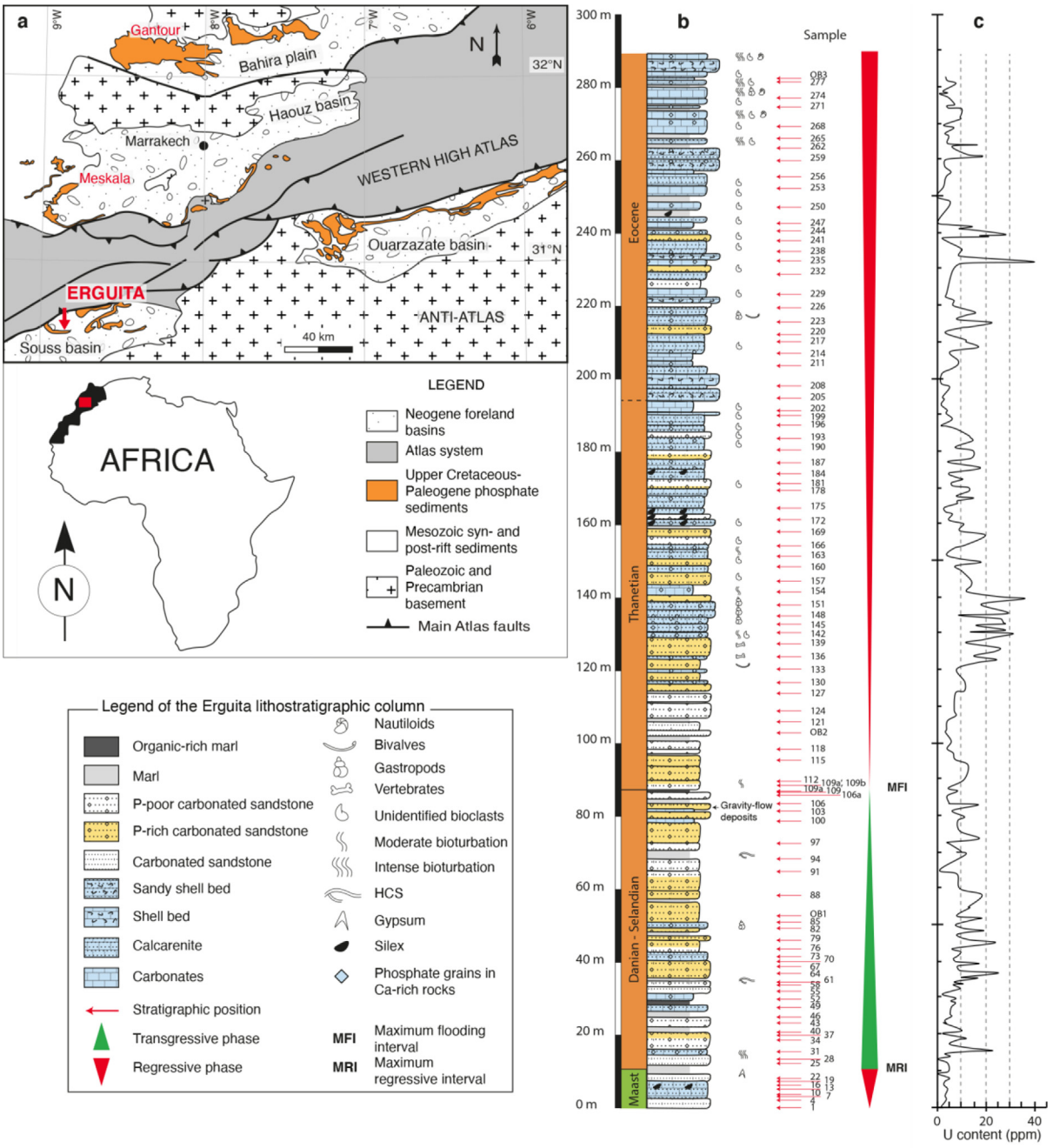

Fig. 1. (a) Simplified structural map of the western High Atlas in Morocco, modified from El Bamiki *et al.* (2020). (b) Detailed lithostratigraphic column of the Erguita section with interpreted regressive and transgressive trends. (c) Gamma-ray curve showing the U content within the sediments. It is assumed that U reflects the proportion of phosphate minerals because of their great incorporation of trace elements, including U, compared to carbonates, sandstones, and marls (Aubineau *et al.*, 2022a; Nathan, 1984).

accumulated on shallow water platforms under the strong influence of Atlantic upwelling currents from the Late Cretaceous to the Eocene (Pufahl and Groat, 2017). They are now preserved within vast plateaus (*e.g.*, Gantour, Ouled Abdoun, and Meskala basins) and along the margins of the western High Atlas (Fig. 1a). The P-rich sediments were bordered by the deformed Variscan basement to the north and east, and by the Paleozoic fold belt of the Anti-Atlas to the south (Herbig and Trappe, 1994). The latter constituted the adjacent hinterland area (El Bamiki *et al.*, 2020). Then, the WHA recorded multiple phases of shortening and uplift with a major event during the Neogene (Frizon de Lamotte *et al.*, 2008, 2009; Lanari *et al.*, 2020; Leprêtre *et al.*, 2018; Missenard *et al.*, 2008). The erosion of the uprising WHA is delivering substantial continental materials to foreland basins (*i.e.*, Haouz, Ouarzazate, and Souss basins), which formed along the northern and southern margins of the orogen (Michard *et al.*, 2008).

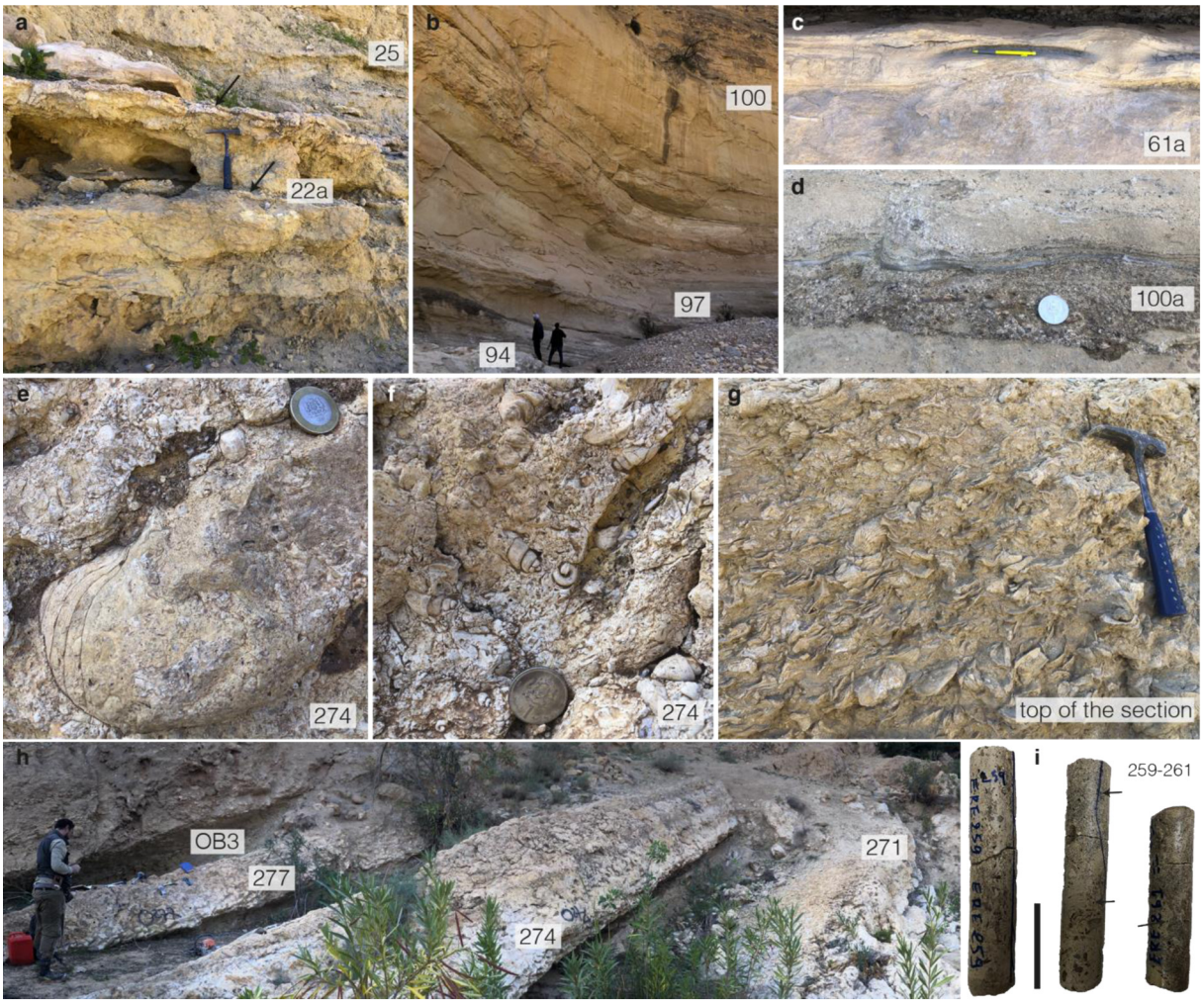

Fig. 2. Facies and sedimentological features. (a) Gypsum layers (arrows) in the basal Erguita section. (b) Massive P-rich carbonated sandstones. Note that these rocks are sometimes crumbly. (c) Hummocky cross-stratification. (d) Finning-upward gravity-flow deposit. (e) Nautiloid. (f) *Turritella* and *Oenopota* gastropods. (g) Massive shell bed composed of oyster fragments. (h) Alternating carbonates and clayey calcarenites in the uppermost part of the section. (i) Example of oriented cylindrical cores consisting of P-rich calcarenite. Arrows show mm-sized, unsorted phosphatic grains. Scale bar: 5 cm. Sample number is indicated in the white rectangle. Coin diameters: 2.4 cm in (d, f) and 2.7 cm in (e). Hammer and pen lengths: 33 and 15 cm, respectively.

2.2 Erguita section

The Erguita section described by Ambroggi in the sixties corresponds to the distal facies of the WHA sedimentary sequences (Ambroggi, 1963). In contrast, shallow proximal facies are found to the east in the Ouarzazate basin (Fig. 1a; El Bamiki *et al.*, 2020). The phosphate-bearing series, first deposited during the Maastrichtian, unconformably overlies Campanian carbonates (Ambroggi, 1963). Based on sedimentological features, sequence stratigraphy, and biostratigraphic data of nannoflora, second-order transgressive-regressive cycles have been successfully described in the WHA between the Late Cretaceous and Eocene (El Bamiki *et al.*, 2020). The Maastrichtian Erguita rocks, consisting of marls and P-poor carbonates accumulated during an episode of sea level rise and fall, are capped by thin gypsum layers (Figs. 1b, 1c, 2a; El Bamiki *et al.*, 2020). The large regression of the late Maastrichtian, leading to the widespread karstification in the eastern part of the WHA has been inferred as the potential event that facilitates gypsum precipitation in proximal environments at Erguita. The overlying Danian-Selandian rocks are mainly characterized by P-rich calcarenites, marls, and thin P-poor carbonated sandstones passing upwards through massive P-rich carbonated sandstones (Figs. 1b, 1c, 2b; El Bamiki *et al.*, 2020). In these sediments, hummocky cross-stratification, interpreted to form within the outer platform between the storm wave-base and the fair-weather wave-base (Burchette and Wright, 1992), and overlying gravity-flow deposits, accumulated below the storm wave-base, indicate a basin deepening (Figs. 1b, 2c, 1d; El Bamiki *et al.*, 2020). Deposition of organic-rich marls in the Erguita section has recorded the maximum flooding interval, a stratigraphic marker interval in the WHA (Fig. 1b; El Bamiki *et al.*, 2020). Then, the basal Thanetian sediments are dominated by turbiditic phosphates, where the phosphatic particles have been transported basinward and rapidly accumulated with a normal grading pattern (Figs. 1b, 1c; El Bamiki *et al.*, 2020).

The greater distance of the Erguita depositional setting from the phosphogenic window and larger detrital inputs diluting phosphate concentrations have led to lower phosphorus enrichment in sediments compared to the Gantour basin, among others (Aubineau *et al.*, 2024a; El Bamiki *et al.*, 2020, 2021, 2023). The progressive deposition of P-containing calcarenites and carbonates, clayey calcarenites, shell beds, and marls, together with the upward increase in faunal content (nautiloids, *Thalassinoides* burrows network, gastropods, bivalves, oysters), characterize the upper part of the section (Figs. 1b, 1c, 2e-2i; El Bamiki *et al.*, 2020). This pattern reflects the regressive phase of the basin, where macroorganisms were likely diversified during the Eocene. During the studied interval, detrital materials and soluble elements probably originated from the emerged Anti-Atlas rocks (El Bamiki *et al.*, 2020; Herbig and Trappe, 1994). Finally, this section is truncated and unconformably covered by Neogene conglomeratic sediments resulting from the erosion of the uprising High Atlas (Ambroggi, 1963; El Bamiki *et al.*, 2020).

3 Material and methods

3.1 Sampling and sample preparation

We sampled 279 oriented cylindrical cores with a portable gasoline-powered rock drill, three oriented blocks with hand sampling techniques (Tauxe *et al.*, 1998), and additional unoriented rocks from the Erguita section in Morocco. All samples from freshly exposed outcrops are in the vicinity of the Erguita riverbed. The coordinates are presented in Table S1. A hundred of stratigraphic levels were studied within the ~290 m thick sedimentary section to characterize the magnetic susceptibility (Fig. 1b). The sampling interval ranges from 0.5 to 6.8 m.

In each of the drilled horizon, three oriented cylindrical cores were collected. The drilling of oriented blocks was carried out at Geosciences Montpellier, University of Montpellier, France. For clarity, sample "1" refers to cylindrical cores number 1, 2, and 3, while "OB" refers to the oriented blocks. We designated unoriented rocks with a letter behind the sample number. For example, sample 109a is therefore located between oriented samples 109 and 112.

We constructed the lithostratigraphic column after carefully examining outcrops, cylindrical cores, the gamma-ray curve, and XRD and geochemical data (Figs. 1b, 1c). We logged all samples to provide information on their stratigraphic position. Standard specimens (2.2 cm in height and 2.5 cm in diameter) from the oriented cylindrical cores and oriented blocks (1–5 per core) were prepared at Geosciences Montpellier, leading to the production of more than 800 specimens. From those cylindrical specimens, 627 were selected (specimens that did not fit into the 3D rotator sample holder were not analyzed) and measured to study the magnetic susceptibility. We crushed and milled by hand in agate mortar representative samples for mineralogical and whole-rock geochemical examination.

3.2 X-ray diffraction

X-ray diffraction (XRD) mineral analyses were performed on powdered bulk samples using a Bruker D8 ADVANCE diffractometer (CuKα radiation) operating at 40 kV and 40 mA to identify the mineralogical phases of P-containing rocks at RRXG platform, University of Montpellier. Analysis of bulk powders was performed over an angular range of 4–62° 2θ and a step size of 0.02° 2θ per 2 s. Bruker Eva software was used for indexing peaks, and XRD patterns were compared with reference data (Brindley and Brown, 1980).

Moreover, Rietveld refinement of XRD patterns allowed a semi-quantification of bulk mineralogy (Tab. 1) using the Profex 4.3.1 interface with the program BGMN (Döebelin and Kleeberg, 2015). Regardless of the software programs used, quantification is challenging when dealing with clay minerals (Hillier, 2000). The accuracy of clay mineral quantification is generally lower than 5 wt.% and up to 10 wt.% when amorphous phases are present (Warr, 2022).

3.3 Whole-rock geochemistry and weathering intensity

We performed whole-rock geochemical analyses of major and trace elements on 10 samples of various lithologies (Tab. 2). Powdered samples were fused with lithium metaborate ($LiBO_2$) for trace and major element measurements (Carignan *et al.*, 2001). Major elements were measured by inductively coupled plasma (ICP) optical emission spectrometry, and trace elements by ICP mass spectrometry at Service d'Analyse des Roches et Minéraux, Nancy, France. Measurement uncertainty and instrument detection limit relative to international standards and sample replicates (Carignan *et al.*, 2001) are provided in Table S2. Reference standards include Basalt BR, anorthosite AN-G, diorite DR-N, serpentinite UB-N, and granite GH (Carignan *et al.*, 2001).

The quantification of the degree of chemical weathering of source rocks was determined by means of the chemical index of alteration (CIA), where $CIA = [Al_2O_3/(Al_2O_3+CaO^*+Na_2O+K_2O) \times 100]$ in mole fraction (Nesbitt and Young, 1982). CaO* is the amount in the silicate fraction. Considering the varying proportions of carbonates and phosphates in the Erguita sedimentary rocks (see Sect. 4.2), CaO* of our samples is assumed with $CaO^* = CaO$ when the mole fraction of CaO is $\leq Na_2O$ and $CaO^* = Na_2O$ when the mole fraction of CaO is $\geq Na_2O$, as previously reported (Jian *et al.*, 2013). Typically, unweathered, moderately weathered, and highly weathered rocks have low (<60), 60–80, and high (>80) CIA values, respectively (Fedo *et al.*, 1995). The pristine phosphatic lithofacies usually show low P_2O_5 contents, while substantial P enrichment within sediments derives from syndepositional repetitive wave and storm winnowing by removing the fine-grained sedimentary detritus (Pufahl and Groat, 2017). As a result, the formation of winnowed phosphates (*i.e.*, phosphate-rich rocks) hinders the calculation of CIA due to potential removal of the silicate fraction (Tab. 2).

3.4 *In situ* gamma-ray spectrometry

Uranium concentrations, used as a proxy for sedimentary phosphate minerals, were measured *in situ* with a portable gamma-ray spectrometer: the Gamma Surveyor Vario (GF Instruments), equipped with a Bismuth Germanium Oxide (BGO; $Bi_4Ge_3O_{12}$) scintillator with 2048 channels, along with a 19 cm^3 detector with probe dimensions of 45 mm and a length of 301 mm (VB1). This equipment allows the

Table 1. Semi-quantification of the mineralogical assemblages in the Erguita sediments. Data were obtained after careful examination of bulk XRD patterns.

Sample	Lithology	Height (m)	Calcite (%)	Dolomite‡ (%)	Dolomite† (%)	CFA (%)	Quartz (%)	K-Feldspar (%)	Smectite (%)	Illite/ Mica (%)	Palygorskite (%)	Chlorite (%)	Kaolinite (%)	Clays total (%)	Gypsum and/or pyrite (%)
OB3	Clayey calcarenite	282.5		25	41	1	15	3		5	8	1		13	1
259	Sandy shell bed	259.9	60		4	15	21								
250	Carbonates	247.1	0.3	46	38	2	3		11					11	
244	P-rich calcarenite	240.6			47	21	26		6					6	
220	Calcarenite	212.4	10	16	40	2	26		5					5	1
214	Carbonates	207.2		0.2	98		2								
181	P-poor, carbonated sandstone	171.3		14	31	1	49	3		1	1			2	
178	Calcarenite	167.6		30	39	1	29	0.4		1				1	1
166	Calcarenite	154.2		20	22	8	45	3		2		1		2	
157	P-rich, carbonated sandstone	144.5	0.1	20	22	9	44	3		1		1		2	
151	Calcarenite	138	3	21	42	8	19	3	4					4	
145	P-rich calcarenite	133			55	23	17	1	4					4	
OB2	P-poor, carbonated sandstone	102.9			43	2	48	3		2			2	4	1
118	P-rich, carbonated sandstone	98.4		14	28	2	50	3		1			1	3	
109b	P-rich, carbonated sandstone	87.6	2	12	15	4	51	5	8				1	10	2
109a’	P-rich, carbonated sandstone	87	2	6	6	5	74	3	5					5	
109a	Marls	86.9		6	9	3	52		11	15			3	29	1
109	P-poor, carbonated sandstone	86.5	5	9	13	8	57	4		1			3	4	
106a	P-poor, carbonated sandstone	85.4	1	13	13	4	56	4	7					7	4
103	Carbonates	81.4		21	62	1	9		7					7	1
100	Carbonates	78.6		25	64	1	8	0.4		1				1	1
64	P-rich, carbonated sandstone	36.9	5		7	27	54	5	2					2	
58	P-poor, carbonated sandstone	33.7	9	2	3	8	69	4		1			2	4	2
55	P-poor, carbonated sandstone	32	1		33	0.1	53	4	7	2				8	2
31	P-rich calcarenite	15.4	1		49	31	14	2	2					2	1
28	P-poor, carbonated sandstone	13.3			29	0.2	58	3		7	2	0.2		9	
25	P-poor, carbonated sandstone	12.2			21	0.2	69	6		2	1	0.4		3	

Dolomite†, Ca-Mg (55:45). Dolomite‡, Ca-Mg (50:50). CFA, carbonate fluorapatite.

Table 2. Major and trace element compositions and CIA values of representative Erguita sediments.

Samples Lithologies	OB3 Clayey calcarenite	250 Carbonates	157 P-rich, carbonated sandstone	118 P-rich, carbonated sandstone	109 P-poor, carbonated sandstone	103 Carbonates	64 P-rich, carbonated sandstone	55 P-poor, carbonated sandstone	31 P-rich calcarenite	28 P-poor, carbonated sandstone
Height (m)	282.5	247.1	144.5	98.4	86.5	81.4.	36.9	32	15.4	13.3
SiO_2 (%)	27.64	5	47.39	53.26	57.01	14.14	51.15	61.13	15.76	59.13.
Al_2O_3 (%)	5.2	0.62	1.91	1.69	1.49	2.28	1.32	2.66	0.64	3.8
Fe_2O_3 (%)	2.04	0.31	0.52	0.6	0.29	0.97	0.32	0.88	0.25	1.3
MnO (%)	b.d.	b.d.	b.d.	0.019	0.018	0.02	b.d.	0.023	b.d.	0.032
MgO (%)	12.03	17.73	7.61	8.2	4.78	15.94	1.46	6.16	9.55	7
CaO (%)	19.28	30.6	17.12	13.55	15.7	24.54	21.95	10.09	33.01	9.61
Na_2O (%)	0.13	0.06	0.15	0.06	0.11	0.07	0.4	0.06	0.48	0.1
K_2O (%)	1	b.d.	0.68	0.66	0.71	0.52	0.79	1.07	0.33	1.51
TiO_2 (%)	0.3	0.034	0.19	0.18	0.12	0.12	0.077	0.28	0.033	0.37
P_2O_5 (%)	1.02	0.65	3.32	0.89	3.31	0.35	10.8	b.d.	11.06	0.17
LOI (%)	30.35	43.69	19.97	19.74	15.01	39.95	9.8	16.15	26.24	16.56
Total	99	98.7	98.9	98.8	98.5	98.9	98.1	98.5	97.4	99.6
CIA	77.5	74.1#	60.6	65.3	57.2	74.3	–	66.4	–	66
La (ppm)	13.15	2	10.23	7.13	10.76	4.41	20.85	7.9	6.83	11.97
Ce (ppm)	23.22	3.3	15.74	13.3	16.68	8.17	26.8	16.18	9.62	24.79
Pr (ppm)	2.98	0.43	2.28	1.72	2.43	1.05	4.38	1.96	1.43	3.02
Nd (ppm)	11.38	1.67	9.24	6.75	10.08	4.14.	18.27	7.43	5.83	11.64
Sm (ppm)	2.27	0.35	1.94	1.44	2.17	0.83	4.03	1.58	1.27	2.41
Eu (ppm)	0.49	0.08	0.45	0.34	0.53	0.19	1.01	0.33	0.33	0.5
Gd (ppm)	1.97	0.33	1.87	1.38	2.13	0.69	4.16	1.45	1.29	2.23
Tb (ppm)	0.3	0.05	0.29	0.23	0.32	0.11	0.62	0.25	0.19	0.37
Dy (ppm)	1.92	0.32	1.91	1.48	2.05	0.69	3.96	1.62	1.21	2.48
Ho (ppm)	0.41	0.07	0.43	0.33	0.46	0.14	0.9	0.36	0.28	0.54
Er (ppm)	1.15	0.19	1.25	0.95	1.28	0.42	2.59	1.03	0.81	1.57
Tm (ppm)	0.17	0.03	0.19	0.15	0.19	0.07	0.37	0.17	0.12	0.25
Yb (ppm)	1.1	0.19	1.32	1	1.22	0.47	2.28	1.19	0.78	1.69
Lu (ppm)	0.17	0.03	0.21	0.16	0.2	0.08	0.37	0.19	0.13	0.27
Y (ppm)	12.79	2.4	16.1	10.21	17.72	4.32	41.38	9.2	11.26	14.19
Zr (ppm)	69.12	18.45	248.9	208.97	186.96	24.69	46.76	348.39	22.83	371.13
(La/Yb)SN	0.88	0.79	0.58	0.53	0.66	0.7	0.68	0.49	0.65	0.53

LOI, loss of ignition; CIA, chemical index of alteration; b.d., below detection ; -, not calculated; #, we used $K_2O = 0.03$, which is the value of the detection limit.

measurement of energies up to 3 MeV. In all studied stratigraphic levels, measurements were acquired by direct probe contact with rock outcrops at planar spots (Table S3). The measurement time was 180 seconds, as recommended by the manufacturer to optimize time and precision.

3.5 Magnetic measurements

Magnetic susceptibility measurements were performed on 627 specimens using an AGICO KLY-5 Kappabridge with an alternative field of 400 A m^{-1} peak value (frequency: 1220 Hz) at the *Géosciences Environnement Toulouse* laboratory (France). We normalized the MS values with respect to the theoretical volume of specimens (10 cm^3). Anisotropy data were processed with the ANISOFT software v.6.1.01 (Chadima and Jelínek, 2008). The ellipsoid of magnetic susceptibility is defined by the orientation and length of the three principal susceptibility axes with K1 > K2 > K3 (Jelinek, 1981). Km represents the mean volume-specific magnetic susceptibility (SI) and reflects the volume content of magnetic minerals in the specimen. The degree of anisotropy (P = K1/K3) represents the intensity of the preferred orientation of magnetic minerals. The T parameter represents the shape of the ellipsoid and varies from −1 (perfectly prolate) to +1 (perfectly oblate). The magnetic lineation (L = K1/K2) is defined by the maximum axis of the ellipsoid, and the magnetic foliation (F = K2/K3) is the plane containing K1 and K2.

3.6 Rock magnetism investigations

Carbonates and carbonated sandstones from the Erguita section carry natural remanent magnetizations with values

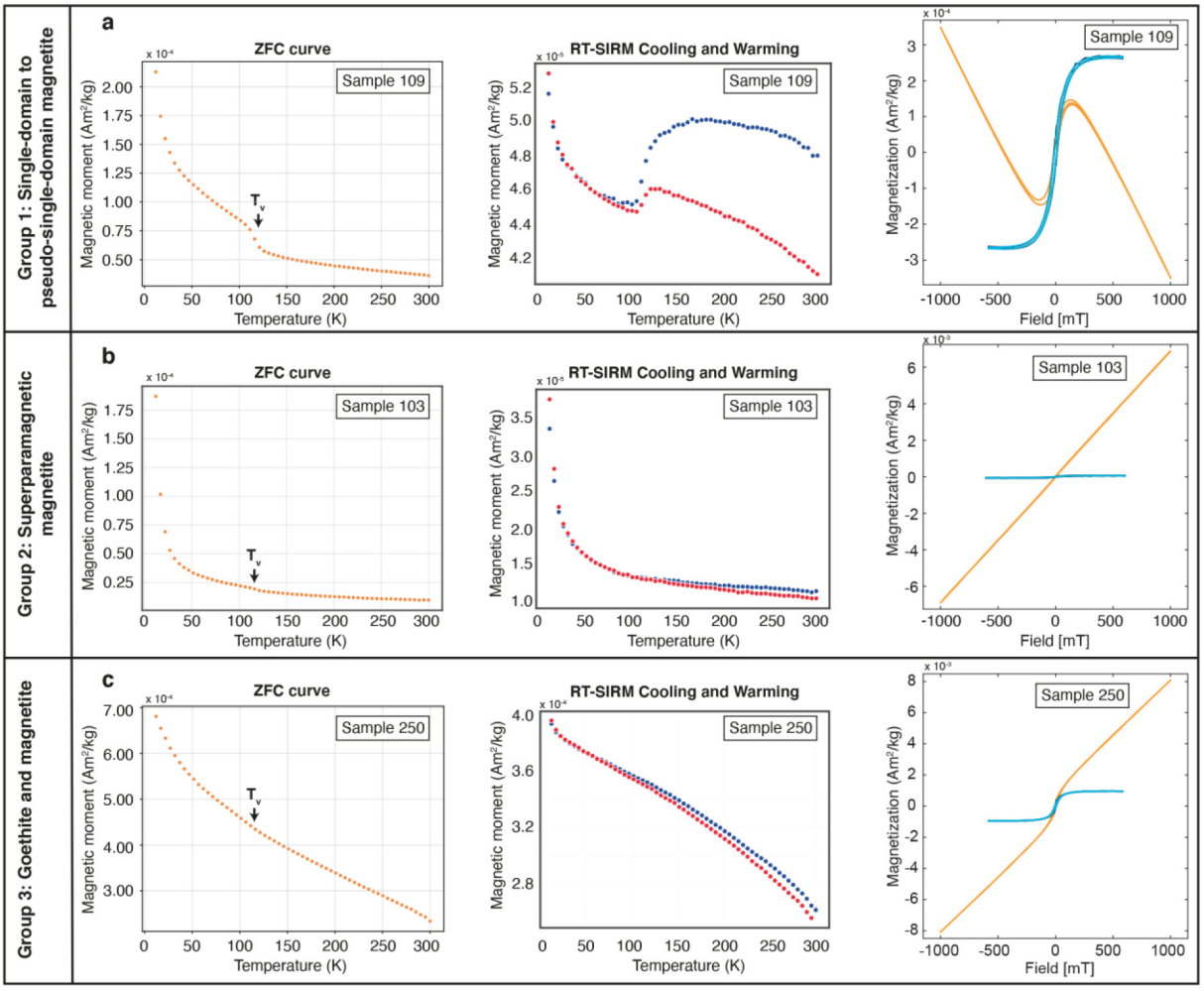

Fig. 3. Rock-magnetism data of the Erguita sediments. (a) Group 1 corresponding to single-domain to pseudo-single-domain magnetite. (b) Group 2 corresponding to superparamagnetic magnetite. (c) Group 3 corresponding to a mixture of iron oxides and iron oxyhydroxide minerals. Left panel, ZFC (zero field cooled) curve with the apparent Verwey transition (Tv); middle panel, mass-normalized RT-SIRM cycles, warming (in red) and cooling (in blue); right panel, uncorrected (orange) and corrected (blue) hysteresis loops.

ranging from 1.8×10^{-10} to 1.9×10^{-09} Am^2 (measurements from 79 oriented core specimens using the Sushibar at LMU Munich). Such rocks with both weak magnetization and weak magnetic susceptibility values (see Results) are challenging to accurately characterize the magnetic mineralogy by means of standard techniques. To tentatively define the magnetic mineralogy, we measured the magnetic hysteresis of six selected samples at room temperature and the low-temperature remanence with a sensitive Quantum Design Magnetic Properties Measurement System (MPMS 3) at the Institute Charles Gerhardt Montpellier (France). The samples were selected along the section to represent stratigraphic levels with strong, intermediate, and weak magnetic susceptibility values. We used the SQUID-VSM configuration of the MPMS3 to achieve a sensitivity, which is lower than 1×10^{-11} Am^2. The bulk fragments were mounted on a clean quartz paddle holder with varnish (sample mass < 50 mg and maximum magnetic moments of the quartz rode measured at room temperature with 2.5 T: 5.6×10^{-10} Am^2). Hysteresis curves were measured at room temperature between -1 and 1 Tesla and processed with HystLab (Paterson *et al.*, 2018). We performed the following low temperature characterization protocol (FC-ZFC-RTSIRMcool-RTSIRMwarm) for the 6 samples (Bilardello and Jackson, 2013): (i) we applied a 2.5 T field during the cooling of the sample followed by the measurement of the remanence until 300 K in zero field (FC, Field-Cooled curve); (ii) next the sample is Zero-Field Cooled and the remanence is measured after applying a short 2.5 T field at low temperatures (ZFC curve); (iii) then, we applied a 2.5 T field at room temperature and we measured the remanence (Room Temperature Saturation Isothermal Remanent Magnetization, RT-SIRM) during the cooling (RT-SIRMcool) and warming to 300 K (RT-SIRMwarm).

4 Results

4.1 Rock magnetism results

At first glance and considering the complexity of measuring rock magnetic data of these rocks, three groups of magnetic mineralogy were determined (see Fig. S2 for the extensive dataset). The first group (including samples 28, 109,

and 166 among the six selected samples) is characterized by samples with a sharp Verwey Transition (Tv) observed at ~120 K (Kosterov, 2002; Özdemir *et al.*, 2002; Verwey, 1935) in both ZFC and RT-SIRM curves, indicating the presence of magnetite as the dominant carrier of the remanent magnetization (Fig. 3a). Moreover, the ZFC curve is above the FC curve, which could suggest a dominance of monodomain grains even if we cannot exclude the presence of pseudo-single domain grains. Indeed, the Mrs/Ms ratios (ratio of remanent saturation moment Mrs to saturation moment Ms) derived from room temperature hysteresis curves show values between 0.08 and 0.12, suggesting a possible pseudo-single domain state rather than single-domain state (Dunlop and Özdemir, 1997). We observe a hump-shaped in the cooling curves between 300 K and the Verwey transition associated to a symmetric hump in the warming curve, which could be associated to the maghemitization, *i.e.*, the partial oxidation of the magnetite particles (Özdemir and Dunlop, 2010). Finally, convergence of FC and ZFC curves around 300 K (Fig. S2) could suggest the presence of goethite in these samples (Taylor *et al.*, 2014). The second group (samples 1 and 103) reveals a faint Tv in the ZFC curve due to magnetite with a downward curvature for the RT-SIRM curves (Fig. 3b). For the sample 103, the magnetic grains seem to be in a superparamagnetic state with no observed coercivity associated to a large remanence drop below 50 K (FC curve). Such smooth and broadened Tv can also be associated to the presence of maghemite. This is consistent with the hypothesis that the finest particles are the most affected by the maghemitization (Özdemir and Dunlop, 2010). Presence of goethite is also suggested by the FC-ZFC convergence after 250 K. The third group (only sample 250) is dominated by the presence of goethite with a characteristic behavior of the reversible RT-SIRM, ZFC, and FC curves (Fig. 3c; Dekkers, 1989). A faint Tv is observed in this sample when looking at the ZFC derivative curve (Fig. S2). The nearly strait with a slight opened loop of the hysteresis curve supports the occurrence of magnetite together with a mixture in the magnetic assemblage (Fig. 3c). It is worth noting that the presence of other iron oxide minerals (*e.g.*, hematite) or pyrrhotite cannot be ruled out with the available data. For example, a small peak at ~250 K for RT-SIRM cool for samples 28 and 166 is observed, but the Morin transition, indicating the presence of hematite (Morin, 1950; Özdemir and Dunlop, 2005), is not supported on the ZFC/FC curves (Fig. S2). Collectively, these rock magnetic data demonstrate the presence of dominant paramagnetic phase as suggested by a steep positive slope of the hysteresis loops associated with a complex ferromagnetic *sensu lato* assemblage with fine magnetite that can be altered in maghemite, and goethite. Presence of pyrrhotite or hematite is not excluded.

4.2 Magnetic susceptibility data and weathering intensity

Depending on the lithology and the number of specimens (3 to 13 per horizon), 2 to 10 measures from different specimens were performed and averaged for each stratigraphic level (Table S4). The P-containing samples studied along the stratigraphic interval of the Erguita section have a mean MS range of -6.2×10^{-6} to $6. \times 8.10^{-5}$ SI (Fig. 4a). Moving upsection, the MS values first show a general increase of 3.1×10^{-5} SI between samples 1 and 28. This is then followed by a progressive upward decrease from the samples 28 to 184, with mean MS values spanning 5.5×10^{-5} to -3.3×10^{-6} SI, before increasing and decreasing again to 2.6×10^{-5} SI (sample 250) and -3.1×10^{-6} (sample 277), respectively. Also, multiple short-term MS fluctuations are observed within these intervals. Finally, the MS values switch to a dramatic ascending increase in sample OB3 with 6.8×10^{-5} SI. Importantly, the MS trends do not vary in response to lithological or long-term eustatic changes. On the other hand, a notable positive relationship is observed between MS and CIA values, as evidenced by an R^2 value of 0.6 and a p-value of 0.02 (Fig. 4b). The average CIA value in the studied section is 68 ± 7, suggesting a moderate level of weathering in the source rocks (Fedo *et al.*, 1995; Nesbitt and Young, 1982).

4.3 Relationships between MS and mineralogical and geochemical contents

Before evaluating the influence of detrital input on MS, we constrained and semi-quantified the mineralogical phases of 27 samples of various lithologies (Fig. S1, Tab. 1). Bulk XRD mineralogical data show that the Erguita sediments mainly comprise two dolomitic minerals and quartz with varying proportions of calcite, carbonate fluorapatite (CFA), and clay minerals. K-feldspar, gypsum, and pyrite appear in small abundances. Typical clay minerals like chlorite, illite/mica, smectite, and kaolinite are observed. In addition, palygorskite, which is a Si- and Mg-rich phyllosilicate (Brindley and Brown, 1980), was mainly detected in the lowermost and uppermost parts of the section (Fig. S1), where the sedimentary succession displays very shallow-water environments. The clay mineralogical assemblage at Erguita is closely similar to the Gantour and WHA lithologies (Aubineau *et al.*, 2022a, 2022b). In general, the XRD mineralogical analysis reveals that siliciclastic detrital material is widespread throughout all lithologies, except two pure carbonate samples.

There is no significant correlation between the proportions of carbonates, quartz, and CFA and the evolution of MS ($R^2 = 0.02$, $p = 0.57$ for carbonates, $R^2 = 0.01$, $p = 0.72$ for quartz, and $R^2 = 0.2$, $p = 0.04$ for CFA). However, the scatter plot between the amount of clay minerals and MS reveals a strong covariation ($R^2 = 0.72$, $p = 0.22$) (Fig. 5). This is coherent with the strong covariation between Al – a detrital indicator – and MS ($R^2 = 0.76$, $p = 0.001$) (Fig. 6a). In addition, the Fe *versus* MS plot indicates that the origin of the MS signal is well supported by Fe-bearing minerals ($R^2 = 0.87$, $p = 7 \times 10^{-5}$) (Fig. 6b). The near-perfect covariation between Al and Fe ($R^2 = 0.95$, $p = 2 \times 10^{-6}$) points to a detrital origin of Fe-bearing minerals (Fig. 6c). Although zircons are presumably detrital grains, the lack of correlation between Zr and MS ($R^2 = 0$, $p = 0.90$) suggests that zircons and magnetic grains were not tightly bound during transportation and deposition of the Erguita sediments (Fig. 6d), which is best explained by their difference in grain size and density.

The PAAS-normalized Rare Earth Element and Yttrium ($REEY_{SN}$, where SN represents values normalized to PAAS) patterns of the Erguita sediments are relatively similar to each other (Fig. 7a), suggesting uptake of REEY from a

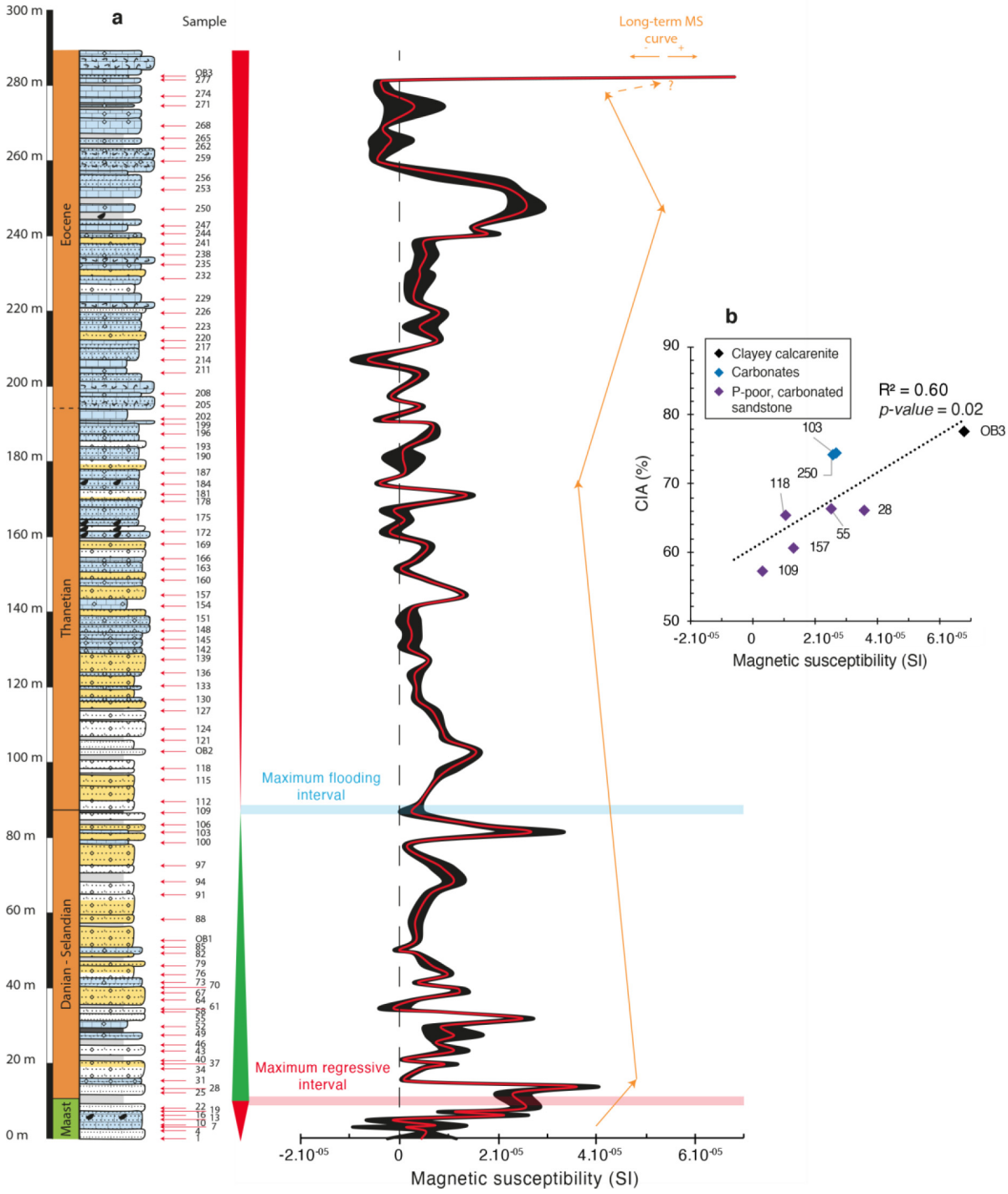

Fig. 4. (a) Magnetic susceptibility curve (SI) with interpreted transgressive-regressive trends in the Upper Cretaceous/Paleogene succession at Erguita. The red line corresponds to the mean MS values, while the black line is the mean MS values with one standard deviation. Legend of the lithostratigraphic column is on Figure 1. The stratigraphy is based on El Bamiki *et al.* (2020). (b) Scatter plot between the chemical index of alteration and magnetic susceptibility. P-rich sediments are not shown because their formation falsifies the CIA values.

geochemically uniform fluid. The $REEY_{SN}$ patterns show light (L)REE depletions relative to heavy (H)REE with $(La/Yb)_{SN}$ values ranging from 0.49 and 0.88 (Fig. 7a; Tab. 2). The latter observation is consistent with the $(Sm/Yb)_{SN}$ and $(Sm/Pr)_{SN}$ ratios plotting on the HREE enriched field (Fig. 7b), excluding middle (M)REE enrichment. Moreover, the $(Ce/Ce^*)_{SN}$ versus $(Pr/Pr^*)_{SN}$ diagram reveals a true negative Ce anomalies in the Erguita sediments (Fig. 7c). Combined, these characteristics yield features akin to those of modern seawater (Alibo and Nozaki, 1999; Bau *et al.*, 1997; Bau and Dulski, 1996;

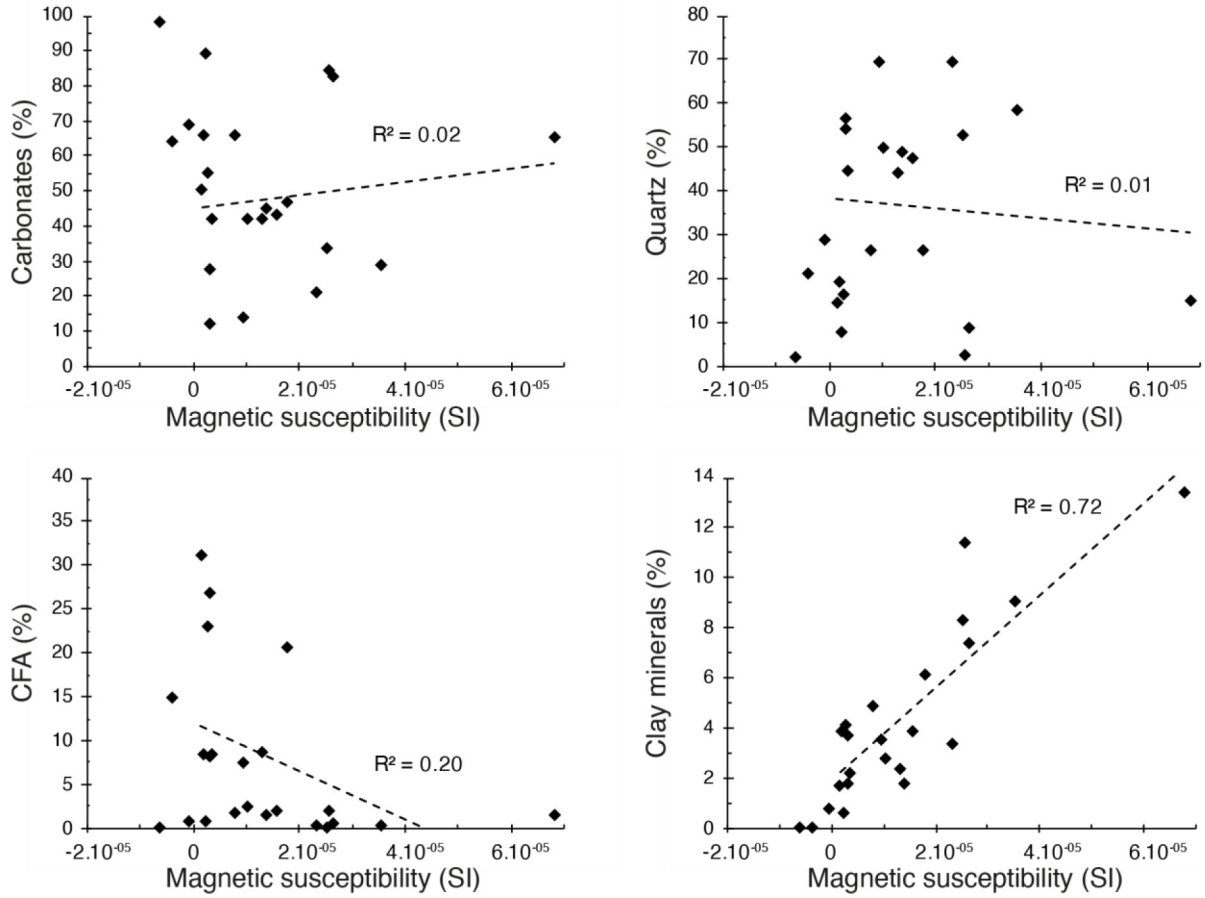

Fig. 5. Relationship between the proportion of most abundant mineral phases and magnetic susceptibility in the Erguita sediments. Linear regressions are shown without the incorporation of negative MS values.

De Baar *et al.*, 1985; Garnit *et al.*, 2012). Besides, the sediments have Y/Ho ratios between 26 and 46, reflecting terrestrial and marine mixing inputs, where Y/Ho ratios >40 and ~26 represent a seawater signal and a strong terrestrial input dominated by fine-grained materials, respectively (Bau *et al.*, 1997). This is further supported by the strong covariation between Y/Ho and Zr in the carbonated sandstones ($R^2 = 0.72$) (Fig. 7d).

5 Discussion

5.1 Diagenetic considerations

Post-depositional processes during diagenesis can alter the primary MS signature. For example, Schneider *et al.* (2004) suggested a genetic link between MS values and Fe-rich carbonates formed during the migration of diagenetic fluids. Although the Erguita limestones are dolomitized, numerous lines of mineralogical and geochemical evidence point to an absence of late'/extensive diagenetic processes that could have erased the detrital MS signal.

Sediments fed by hydrothermal fluids are usually enriched in Fe (*e.g.*, Chavagnac *et al.*, 2018; Clarkson *et al.*, 2014), leading to an absence of covariation between Al and Fe. No such decoupling was observed in the Erguita sediments. Instead, the strong correlations between Al, Fe, and MS reflect the detrital prevalence of magnetic minerals. Bulk XRD patterns do not show illite/smectite mixed-layer minerals. The absence of such minerals in other WHA sections (Aubineau *et al.*, 2022a; Knidiri *et al.*, 2014) indicates minimal diagenetic transformations within the sediment pile (Środoń and Eberl, 1984; Velde *et al.*, 1986). Besides, elevated CFA-hosted CO_3^{2-}concentrations characterize the P-containing Erguita samples, where they averaged 5.9 ± 1.6 (1σ, $n = 13$) (Tab. S5, method of calculation presented in Schuffert *et al.* (1990), comparable to the 4–8 wt.% CO_3^{2-}content of Moroccan CFA grains (Aubineau *et al.*, 2024b, 2022b, 2022a; Cosmidis *et al.*, 2013; El Bamiki *et al.*, 2023; Kocsis *et al.*, 2014; Nguidi *et al.*, 2021). This trend results from the equilibrium of CFA with seawater (Nathan, 1984), while thermal diagenesis and weathering result in progressive decarbonation of CFA toward fluorapatite composition (*i.e.*, nearly zero CO_3^{2-}substitution) (McClellan and Van Kauwenbergh, 1991).

Furthermore, the REEY distribution in sedimentary rocks allows the evaluation of seawater chemistry in depositional settings. REEY typically exhibit a conservative behavior (*i.e.*, no fractionation) during sediment deposition (*e.g.*, Bau and Dulski, 1996; Shields and Stille, 2001). The REEY pattern and composition in the Erguita sediments agree with deposition in fully oxygenated seawater (Alibo and Nozaki, 1999; Bau *et al.*, 1997; Bau and Dulski, 1996; De Baar *et al.*, 1985). MREE enrichment with respect to LREE and HREE (Reynard *et al.*, 1999), caused by anoxic porewaters or late diagenetic fluids as

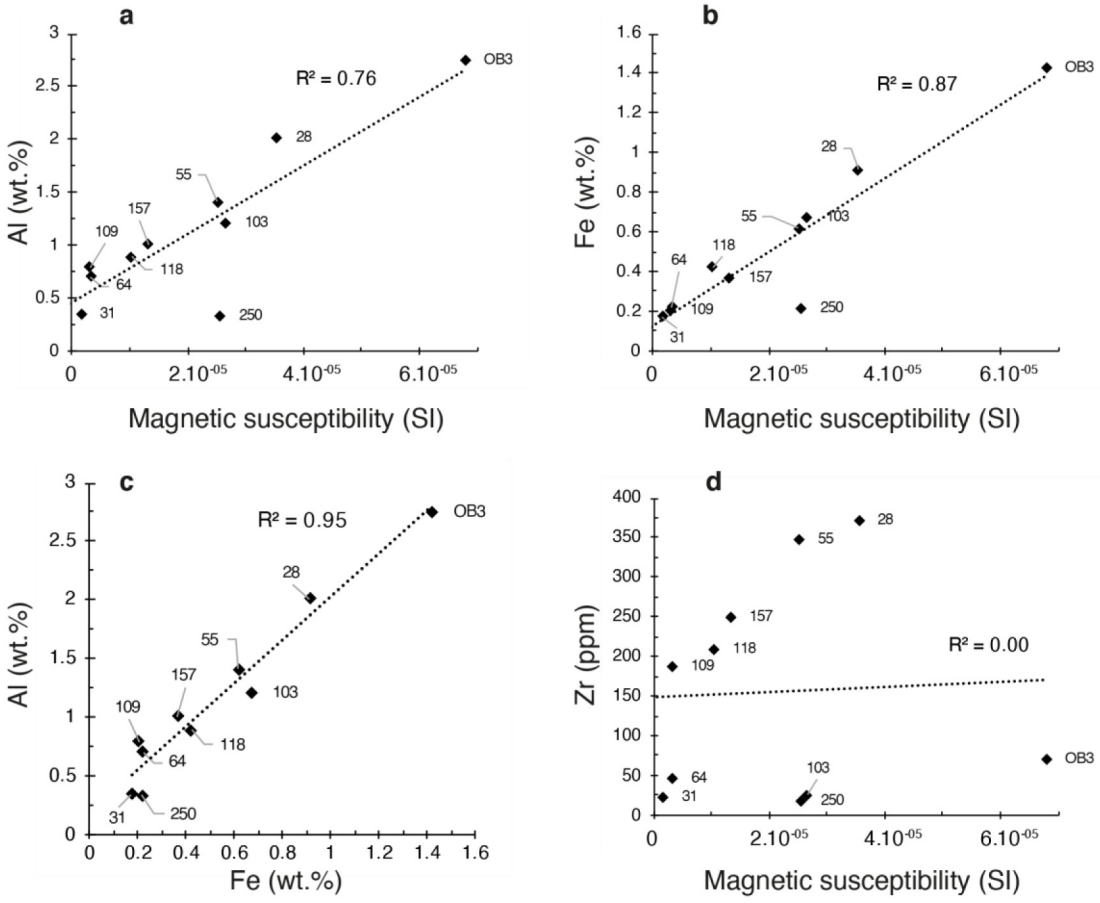

Fig. 6. Scatter plots showing the relationships between Al and MS (a), Fe and MS (b), Al and Fe (c), and Zr and MS (d).

a source of REEY is not observed in our samples. The $(La/Yb)_{SN}$ ratios ranging from 0.5 to 0.9 in the Erguita sediments compared to 0.4–0.5 for modern seawater suggest adsorption mechanisms (Reynard *et al.*, 1999). The negative correlation between Zr and Y/Ho, together with Y/Ho ratios being more similar to clastic sediment values, hint that REEY values are also influenced by siliciclastic detritus derived from continental weathering. Therefore, we interpret the REEY distribution at Erguita to mirror the chemical composition of seawater, from which terrestrial REEY fluxes via continental runoff were sourced to the depositional environments. Also, the REEY probably adsorbed onto the siliciclastic detritus.

In light of the above considerations, the MS signal in this study is primarily attributed to detrital sources. Thus, the Erguita MS data can be reliably used for paleoenvironmental and/or paleoclimatic reconstructions.

5.2 Origin of the magnetic susceptibility variations

The rock magnetism of representative Erguita rocks has revealed that there is no correlation between the magnetic mineralogy and variations in magnetic susceptibility since the magnetite-bearing samples of the first group show both high and low MS values. The MS signal at Erguita does not correspond to the lithological changes, but instead shows a consistent relationship with the amount of clay mineral present in the entire section. The MS changes could be attributed to variations of paramagnetic mineral proportions, such as Fe-bearing phyllosilicates. However, the dominant presence of Fe-free palygorskite $[Si_8O_{20}(Mg_2Al_2)(OH)_2(OH_2)_4 \cdot 4H_2O]$ (Singer and Galan, 1984) associated with the highest MS value in the upper part of the section does not fully support the relationship between MS and paramagnetic mineral content. Collectively, the data suggest that the proportion of more or less oxidized magnetite supplied to the depositional setting controls the MS variations at Erguita.

The covariation between MS and clay mineral content likely indicates that ferromagnetic *sensu lato* minerals and phyllosilicates were supplied together to the depositional setting. The Erguita samples show a magnetic fabric typical of sedimentary rocks (type 1 according to Aubourg *et al.*, 2004), which is revealed by the high inclination of K3 axes and the random distribution of K1 and K2 axes within the horizontal plane (Fig. 8a). Figure 8 shows that the magnetic foliation of the mean average of all sites from the Erguita section is oblique to the bedding plane by ~24°, whereas the K1 axis is perpendicular to the K3 direction. At first order, there is an overall consistency across the ~290 m-thick section. Such AMS fabric suggest that the particles are rolled and transported from the SE to the NW if we assume the K3 axis as an indicator of paleocurrent direction. A site-by-site analysis shows a

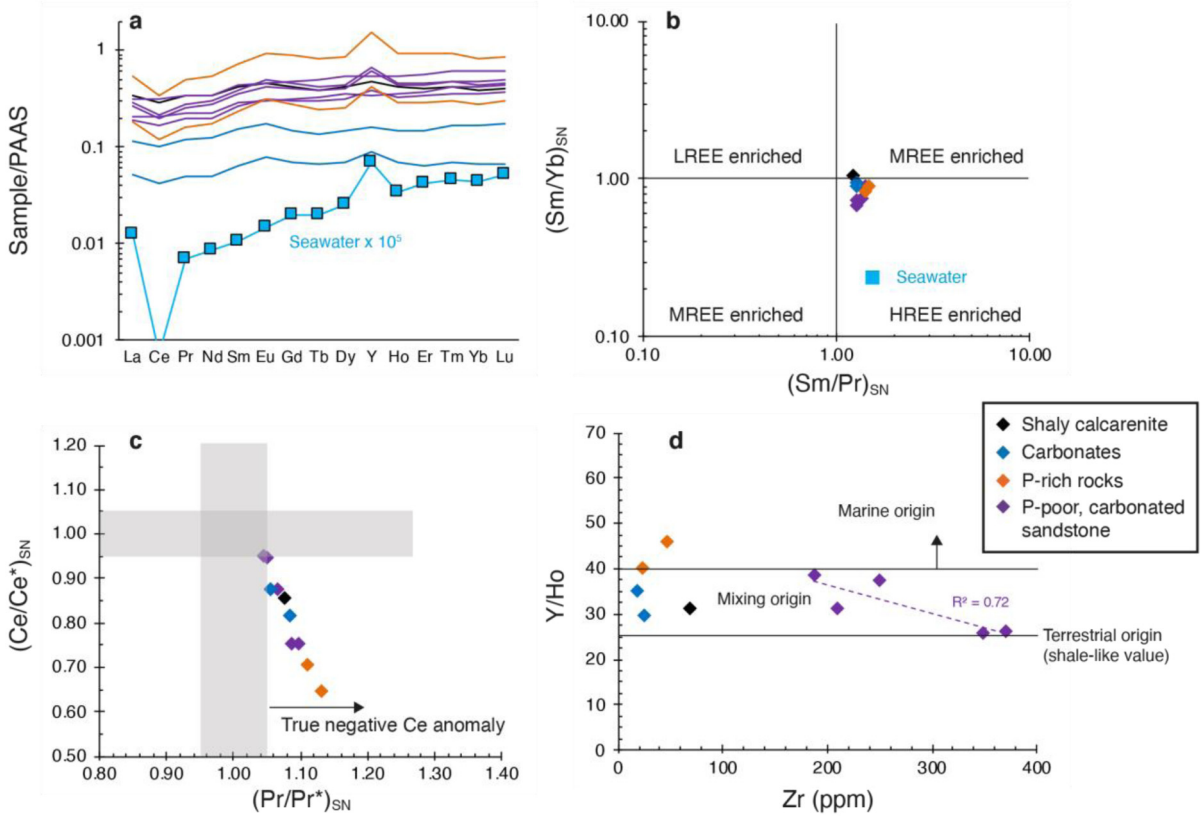

Fig. 7. REEY geochemistry of the Erguita section. (a) Average PAAS-normalized REEY patterns compared to modern seawater (Alibo and Nozaki, 1999). Light (L)REE (La to Nd), Middle (M)REE (Sm to Dy), and Heavy (H)REE (Ho to Lu). Geochemical data of PAAS are from Taylor and McLennan (1985). (b) $Sm/Yb)_{SN}$ *vs.* $(Sm/Pr)_{SN}$, after Garnit *et al.* (2012). Data of SW are from Alibo and Nozaki (1999). (c) Ce anomaly *vs.* Pr anomaly, after Bau and Dulski (1996). (d) Cross plot between Y/Ho and Zr showing the source of REE within the depositional environments. The Y/Ho ratios indicate a mixing source of REE.

tendency with a predominance of oblate-type ellipsoid when the fabric is very well defined. The main AMS fabric may reflect the behavior of the different paramagnetic phases in the samples, as suggested by the rock magnetic data (Fig. S2). Moreover, for the specimens dominated by a ferromagnetic *sensu lato* assemblage (*e.g.*, sample 166), the corresponding AMS may reflect the behavior of oxidized magnetite associated to goethite particles. The samples were further divided into two subpopulations, representing the phyllosilicate proportion (Fig. S3). The Al-rich samples (*i.e.*, high proportion of clay minerals) show a more oblate fabric parallel to the bedding plane in agreement with the platy morphologies of the phyllosilicates compared to the Al-poor samples (*i.e.*, low proportion of clay minerals). The K3 axis for the Al-rich samples are plunging to the N with a slight imbrication. After removing the specimen with high-anisotropy value (ERA31A), the fabric of the Al-poor samples is better defined with a fabric close to the Al-rich subpopulation with an imbrication to the NW. Despite a wide dispersion, the K1 is relatively aligned to the K3 direction. Given the lack of sedimentary evidence to provide a paleocurrent orientation, the dominant direction of the K3 axes to the NW could be used as a first indicator.

We hypothesize the emerged Anti-Atlas crystalline basement to the SE as a source of detrital materials to the Erguita depositional environment, as already suggested by El Bamiki *et al.* (2020) and Herbig and Trappe (1994). Thus, one process occurring on the Anti-Atlas Mountains should exclusively explain the simultaneous delivery of clay and ferromagnetic minerals to the depositional sites. Some sites (52, 100, 229, 247, 250) show an inverse fabric with horizontal K3 in Figure 8. The hypotheses to explain the origin of such inverse AMS fabric include the occurrence of (i) single-domain magnetite (Potter and Stephenson, 1988), (ii) high susceptibility minerals as maghemite (Borradaile and Puumala, 1989), (iii) greigite and some suitable titanomagnetite compositions (Aubourg and Robion, 2002).

Autocyclic physical processes, including tidal current and wave and storm winnowing, are superimposed on tectono-eustatic-climatic allocyclic forcing (Walker and James, 1992). Inherent to the depositional system, the former processes over short-time and temporal scales may reduce the visibility of the expected long-term allocyclic variations. With this in mind, hydrodynamic winnowing, reworking, and transporting that have led to the *in situ* phosphate enrichment in the Erguita sediments (El Bamiki *et al.*, 2020) may have been an important controlling factor. These hydrodynamic processes could have thus removed the ferromagnetic and paramagnetic fractions, increasing and decreasing the CFA content and MS values, respectively. In the Moroccan phosphate-bearing rocks, uranium is mainly hosted by CFA (Aubineau *et al.*, 2022a). In addition to

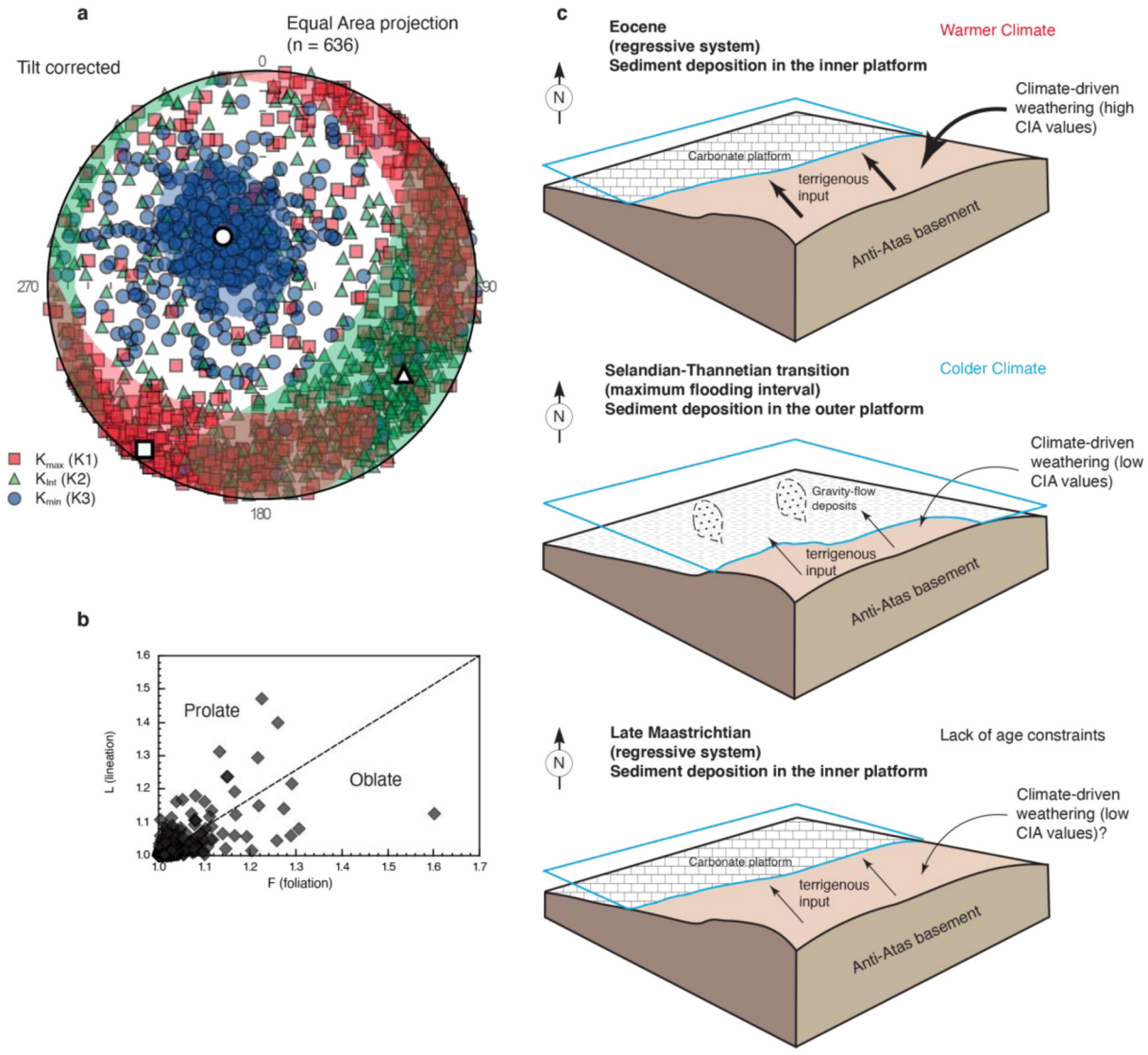

Fig. 8. (a) Data plotted on a lower hemisphere stereonet projection showing the magnetic grain fabric. This projection derives from the AMS ellipsoid (for a comprehensive illustration see Zhang *et al.* (2010) and Bilardello (2021). K_{min} is vertical and K_{max} and K_{int} axes are randomly distributed within the horizontal plane, which indicates deposition of particles under gravity only. (b) Flinn diagram (Flinn, 1978) of AMS data showing a minimum degree of anisotropy due to the presence of both oblate (disk-shaped) and prolate (rod-shaped) particles. (c) 3D paleogeographic model illustrating the weathering intensity that controls the magnetic mineral proportions between the late Maastrichtian and Eocene. In this study, sea level changes and MS vary independently. Both phyllosilicates and ferromagnetic minerals likely contribute to the MS signal.

U, P_2O_5 concentration is a tracer for CFA enrichment. Combined, these proxies allow to decipher whether the autocyclic processes led to the observed MS variations in the Erguita section. The relationships between CFA abundance, U and P_2O_5 concentrations, and associated MS are weak, as shown in Figure 5 and Figure S4. This strongly supports that mechanical winnowing/reworking, resulting in the phosphate enrichment in sedimentary environments, along the Atlantic Paleogene passive margin did not intensively contribute to the expression of MS values.

Weathering drives the delivery of siliciclastic material from the land to oceans (Walker *et al.*, 1981). Global tectonic, sea-level, and climate changes strongly influence weathering regimes. Thus, such events should exert considerable pressure on the flux of magnetic minerals. Considering the relative tectonic stability in northwestern Morocco between the late Cretaceous and Paleogene (Charton *et al.*, 2021), the onset of the Africa-Eurasia convergence did not influence the MS values. The amount of detrital particles transported from land to oceans could have increased during times of regression (Crick *et al.*, 1997; Ellwood *et al.*, 1999). In this scenario, sea level fall leads to a lowering of the base level, which in turn increases erosion. However, our results show a long-term decreasing MS trend in both sea level rise and fall, hinting that eustatic fluctuations over millions of years did not influence the MS trend in the Erguita section.

In contrast, MS values correlate well with CIA – a proxy of weathering intensity, suggesting a direct connection

between climate change and MS. Nonetheless, the CIA values of sedimentary rocks may be prone to unavoidable limitations (Fedo and Babechuk, 2022; Meunier *et al.*, 2013). Besides, the omission of SiO_2 content in the CIA calculation, the composition of the source rock and the effect of K addition during diagenesis can potentially influence the CIA index. Typically, mafic igneous rocks rich in ferromagnesian content can generate misleading interpretations (Fedo and Babechuk, 2022). In other words, the CIA index must be used to the study of feldspar-hosted rocks of the upper continental crust and derived sediments. The Erguita sedimentary rocks fulfill this criterion as we observe a felsic provenance with related minerals like K-feldspar and quartz (Fig. S1). Our observations indicate that the CIA values are reliable.

The upper Erguita sequence of Eocene age (El Bamiki *et al.*, 2020) shows the highest CIA and MS values. The climate state in the Paleogene was highly dynamic with long-term warming (*e.g.*, early Danian) and cooling (*e.g.*, mid-Danian to early Thanetian) periods (Westerhold *et al.*, 2020). In addition, a 9-million-years unprecedented hothouse state occurred during the early Eocene – also known as the Early Eocene Climatic Optimum (EECO), when temperatures were $>10\,^{\circ}C$ warmer than today. As a corollary, the rise of atmospheric CO_2 concentrations increases temperature and precipitation, thereby enhancing chemical weathering (Walker *et al.*, 1981; Warr, 2022). In the upper Erguita section, we propose that the EEOC possibly drove up the supply of detrital magnetic components to the shallow waters. Also, our model should imply any relationship between low CIA, MS values, and colder temperatures. This pattern seems to be preserved during the maximum flooding interval at the Selandian-Thanetian transition (Fig. 4) when temperatures were the coolest of the Paleocene (Westerhold *et al.*, 2020). Considering this, our data indicate that the intensity of weathering induced by climate has a significant impact on the long-term evolution of MS. (Fig. 8c). Our work does not rule out the possibility of minor controls exerted by sea level changes on MS trend during high-frequency perturbations, as proposed by Whalen and Day (2010).

5.3 Implications for paleoenvironmental and paleoclimatic reconstructions at the Cretaceous/Paleogene transition

Our combined analyses of rock magnetism, mineralogy, and geochemistry show that MS in an adequate proxy of the long-term evolution of weathering intensity. Understanding the MS evolution has considerable implications for unraveling processes that drove the low MS signal in the decimeter-thick sediments immediately underlying the K-Pg boundary (*e.g.*, Abrajevitch *et al.*, 2015; Font *et al.*, 2011; Lowrie *et al.*, 1990). To explain this low MS interval, unresolved debates suggest a post-depositional dissolution of ferromagnetic minerals (Lowrie *et al.*, 1990) or an increase in atmospheric and oceanic acidity linked to Deccan Traps volcanism (Abrajevitch *et al.*, 2015) to explain this low susceptibility interval. The putative discovery of chloride-rich iron oxyhydroxides (*i.e.*, akaganeite) in stratigraphic horizons of low MS values below the K-Pg boundary from three distinct European sections could confirm the latter view (Font *et al.*, 2017). Primary akaganeite formation requires large concentrations of both dissolved ferrous iron and chloride ions, acidic and oxidizing conditions, and elevated temperatures (Johnston, 1977; Schwertmann and Cornell, 1991). Such conditions are typically observed in hydrothermal deposits of the Mid-Atlantic ridge (Bogdanov *et al.*, 2008; Chavagnac *et al.*, 2018). In contrast, the Late Cretaceous akaganeite could have been formed in the acidic and chloride-rich Deccan volcanic plume and subsequently transported several thousands of kilometers away as aerosols (Font *et al.*, 2017). However, linking low MS values to global environmental acidification triggered by Deccan volcanism in stratigraphic horizons containing Cl-rich iron oxyhydroxides may not be straightforward. This is because the akaganeite formation and the mechanism responsible for the MS decrease could have occurred independently.

Our study emphasizes that the decrease of magnetic mineral content (*i.e.*, lower MS values) immediately underlying the K-Pg boundary could now be interpreted differently, although no direct evidence for relationships between MS signal and weathering intensity over a few thousand years has so far been documented. This is further supported by previous assessments of CIA in the Yacoraite and Mingshui formations from northwestern Argentina and northeastern China, respectively (Gao *et al.*, 2021; Rohais *et al.*, 2019). These sediments have recorded a decrease in chemical weathering intensity prior to the K-Pg boundary. Furthermore, oxygen isotopic compositions of the Bidart (France) section correlated with those of the South Atlantic deep-sea site indicate a climate cooling in sediments containing the low MS interval during the last thousands of years of the Maastrichtian (Font *et al.*, 2014; Li and Keller, 1998). Consequently, the weathering intensity could have decreased, leading to reduced delivery of magnetic minerals from land to the oceans. Therefore, it is important to use caution when interpreting MS data with regard to paleoenvironmental changes, such as global environmental acidification. The low weathering intensity and MS values before the K-Pg boundary could provide evidence of a mechanistic link between MS and weathering regime over thousand-year timescales.

6 Conclusion

Combined magnetic susceptibility, mineralogical, and geochemical investigations are presented here for the continuous Upper Cretaceous/Paleogene Erguita sedimentary sequence. Moderate chemical weathering would have facilitated the supply of magnetic detritus (both Fe-bearing phyllosilicates and ferromagnetic *sensu lato* minerals) to the oceans (Fig. 8c). These minerals may have been inherited from weathered parent rocks, sediments, or soils of the Anti-Atlas. Our observations hint that the evolution of magnetic susceptibility over millions of years in the Erguita section correlates with weathering intensity as a response to the Paleogene climate change. This work provides evidence for a new weathering proxy. We conclude that the Moroccan Erguita section could offer new insights into the origin of the low susceptibility zone at the K-Pb boundary.

Acknowledgments

Thanks to the scientific board of Geoscience Montpellier for supporting this work. The University of Mohammed VI Polytechnic is deeply thanked for field-trip logistics. We are grateful to Bernard Fraisse for his technical assistance during XRD measurements at RRXG platform of University of Montpellier. We would also like to thank Corine Reibel for her technical expertise and the MPMS measurements at IGCM.

Supplementary material

Figure S1: XRD patterns of randomly oriented bulk powders of Erguita P-containing sediments. All XRD patterns are shown with the same intensity scale. All lithologies are presented

Figure S2: Raw magnetic susceptibility curve and associated rock magnetism dataset. Group 1 is composed of samples 28, 109, and 166. Group 2 is composed of samples 1 and 103, whereas Group 3 is only composed of sample 250. (I) Uncorrected (orange) and corrected (blue) hysteresis loop at room temperature. (II) Detail in blue of the corrected hysteresis loop. (III) Compilations of the ZFC, FC, RT-SIRM curves. (IV) ZFC curve (red) with its associated first derivative (blue). (V) RT-SIRM cycles. (VI) Detailed of the ZFC curve to observe the Verwey transition at ~120 K.

Figure S3: AMS fabric differentiated by the whole-rock Al_2O_3 content (right panels, <2 %; left panels, >2 %). In the Erguita section, the Al_2O_3 content reflects the clay mineral proportion. (a) Data plotted on a lower hemisphere stereonet projection. (b) Jelinek plot showing the shape parameter T versus the corrected degree of anisotropy P (Jelinek, 1981).

Figure S4: Scatter plots between U content, P_2O_5, and MS.

Table S1: GPS coordinates of sampled outcrops, including cylindric cores and oriented blocks.

Table S2: Uncertainty and detection limit of each analyzed element.

Table S3: U concentrations obtained by gamma-ray spectrometry.

Table S4: Mean MS values and associated standard deviations of the Erguita oriented cylindrical cores.

Table S5: XRD reflections and estimated CO_3^{2-} contents (wt.%) of representative P-containing Erguita sediments. The carbonate concentration (wt.%) in CFA grains is calculated as $10.643x^2 - 52.512x + 56.986$ where x stands for $\Delta 2\theta(004\text{-}410)$.

The Supplementary Material is available at https://www.bsgf.fr/10.1051/bsgf/2024025/olm.

References

Abrajevitch A, Font E, Florindo F, Roberts AP. 2015. Asteroid impact vs. Deccan eruptions: The origin of low magnetic susceptibility beds below the Cretaceous-Paleogene boundary revisited. Earth Planet Sci Lett 430: 209–223.

Alibo DS, Nozaki Y. 1999. Rare earth elements in seawater: particle association, shale-normalization, and Ce oxidation. Geochim Cosmochim Acta 63: 363–372.

Ambroggi R. 1963. Etude géologique du versant méridional du Haut Atlas occidental et de la plaine du Souss. Université de Paris, Paris.

Aubineau J, Parat F, Chi Fru E, El Bamiki R, Mauguin O, Baron F, Poujol M, Séranne M. 2022a. Geodynamic seawater-sediment porewater evolution of the east central Atlantic Paleogene ocean margin revealed by U-Pb dating of sedimentary phosphates. Front Earth Sci 10: 997008.

Aubineau J, Parat F, Elghali A, Raji O, Addou A, Bonnet C, Muñoz M, Mauguin O, Baron F, Jouti MB, Yazami OK, Bodinier J-L. 2022b. Highly variable content of fluorapatite-hosted CO_3^{2-} in the Upper Cretaceous/Paleogene phosphorites (Morocco) and implications for paleodepositional conditions. Chem Geol 597: 120818.

Aubineau J, Parat F, Pierson-Wickmann A-C., Séranne M, Fru EC, El Bamiki R, Elghali A, Raji O, Muñoz M, Bonnet C, Jourani E-S., Yazami OK, Bodinier J-L. 2024a. Phosphate δ13Corg chemostratigraphy from the Gantour basin, Morocco: a proof of concept from the K-Pg transition to mid-Thanetian. Chem Geol 121861.

Aubineau J, Séranne M, Chi Fru E, Poujol M, El Bamiki R, Antonio PYJ, Muñoz M, Elghali A, Raji O, Jourani E-S., Bodinier J-L., Parat F. 2024b. Deciphering the U-Pb dates of sedimentary phosphates: a complex example from the Upper Cretaceous-Lower Paleogene series in northwestern Morocco. Chem Geol 661: 122178.

Aubourg C, Robion P. 2002. Composite ferromagnetic fabrics (magnetite, greigite) measured by AMS and partial AARM in weakly strained sandstones from western Makran, Iran. Geophys J Int 151: 729–737.

Aubourg C, Smith B, Bakhtari K, Guya N, Eshragi A, Lallemant S, Molinaro M, Braud X, Delaunay S. 2004. Post-Miocene shortening pictured by magnetic fabric across the Zagros-Makran syntaxis (Iran), in: *Orogenic Curvature: Integrating Paleomagnetic and Structural Analyses*, edited by A.J. Sussman, A.B. Weil. Geological Society of America Special paper, pp. 11–4à.

Averbuch O, Tribovillard N, Devleeschouwer X, Riquier L, Mistiaen B, Van Vliet-Lanoe B. 2005. Mountain building-enhanced continental weathering and organic carbon burial as major causes for climatic cooling at the Frasnian-Famennian boundary (c. 376 Ma)? Terra Nova 17: 25–34.

Bau M, Dulski P. 1996. Distribution of yttrium and rare-earth elements in the Penge and Kuruman iron-formations, Transvaal Supergroup, South Africa. Precamb Res 79: 37–55.

Bau M, Möller P, Dulski P. 1997. Yttrium and lanthanides in eastern Mediterranean seawater and their fractionation during redox-cycling. Mar Chem 56: 123–131.

Bilardello D. 2021. Late Paleozoic Depositional Environments and Sediment Transport Directions of the Itararé Group Rocks From the State of São Paulo, Brazil, Determined From Rock Magnetism and Magnetic Anisotropy. Earth Space Sci 8: e2021E A001703.

Bilardello D, Jackson M. 2013. Cover article: What do the Mumpsies do? IRM Quarterly 23.

Bogdanov YuA, Vikent'ev IV, Lein AYu, Bogdanova OYu, Sagalevich AM, Sivtsov AV. 2008. Low-temperature hydrothermal deposits in the rift zone of the Mid-Atlantic Ridge. Geol. Ore Deposits 50: 119–134.

Borradaile GJ, Puumala MA. 1989. Synthetic magnetic fabrics in a plasticene medium. Tectonophysics 164: 73–78.

Boulila S, de Rafélis M, Hinnov LA, Gardin S, Galbrun B, Collin P-Y. 2010. Orbitally forced climate and sea-level changes in the Paleoceanic Tethyan domain (marl-limestone alternations, Lower Kimmeridgian, SE France). Palaeogeogr Palaeoclimatol Palaeoecol 292: 57–70.

Boulila S, Galbrun B, Hinnov LA, Collin P-Y. 2008. Orbital calibration of the Early Kimmeridgian (southeastern France): implications for geochronology and sequence stratigraphy. Terra Nova 20: 455–462.

Brindley GW, Brown G. 1980. Crystal structure of clay minerals and their X-ray identification. Mineralogical Society, London.

Burchette TP, Wright VP. 1992. Carbonate ramp depositional systems. Sediment Geol 79: 3–57.

Carignan J, Hild P, Mevelle G, Morel J, Yeghicheyan D. 2001. Routine analyses of trace elements in geological samples using flow injection and low pressure on-line liquid chromatography coupled to ICP-MS: a study of geochemical reference materials BR, DR-N, UB-N, AN-G and GH. Geostandards Newsletter 25: 187–198.

Chadima M, Jelínek V. 2008. Anisoft 4.2. – Anisotropy data browser. Paleo, Rock and Environmental Magnetism, 11th Castle Meeting. Contrib Geophys Geodesy.

Charton R, Bertotti G, Arnould AD, Storms JEA, Redfern J. 2021. Low-temperature thermochronology as a control on vertical movements for semi-quantitative source-to-sink analysis: a case study for the Permian to Neogene of Morocco and surroundings. Basin Res 33: 1337–1383.

Chavagnac V, Leleu T, Fontaine F, Cannat M, Ceuleneer G, Castillo A. 2018. Spatial Variations in Vent Chemistry at the Lucky Strike Hydrothermal Field, Mid-Atlantic Ridge (37°N): Updates for Subseafloor Flow Geometry From the Newly Discovered Capelinhos Vent. Geochem Geophys Geosyst 19: 4444–4458.

Clarkson MO, Poulton SW, Guilbaud R, Wood RA. 2014. Assessing the utility of Fe/Al and Fe-speciation to record water column redox conditions in carbonate-rich sediments. Chem Geol 382: 111–122.

Cosmidis J, Benzerara K, Gheerbrant E, Estève I, Bouya B, Amaghzaz M. 2013. Nanometer-scale characterization of exceptionally preserved bacterial fossils in Paleocene phosphorites from Ouled Abdoun (Morocco). Geobiology 11: 139–153.

Crick RE, Ellwood BB, Hassani AE, Feist R, Hladil J. 1997. MagnetoSusceptibility Event and Cyclostratigraphy (MSEC) of the Eifelian-Givetian GSSP and associated boundary sequences in north Africa and Europe. Episodes J Int Geosci 20: 167–175.

Da Silva AC, De Vleeschouwer D, Boulvain F, Claeys P, Fagel N, Humblet M, Mabille C, Michel J, Sardar Abadi M, Pas D, Dekkers MJ. 2013. Magnetic susceptibility as a high-resolution correlation tool and as a climatic proxy in Paleozoic rocks – merits and pitfalls: examples from the Devonian in Belgium. Mar Petrol Geol 46: 173–189.

Da Silva A-C., Mabille C, Boulvain F. 2009. Influence of sedimentary setting on the use of magnetic susceptibility: examples from the Devonian of Belgium. Sedimentology 56: 1292–1306.

Da Silva A-C., Sinnesael M, Claeys P, Davies JHFL, de Winter NJ, Percival LME, Schaltegger U, De Vleeschouwer D. 2020. Anchoring the Late Devonian mass extinction in absolute time by integrating climatic controls and radio-isotopic dating. Sci Rep 10: 12940.

Da Silva AC, Whalen MT, Hladil J, Chadimova L, Chen D, Spassov S, Boulvain F, Devleeschouwer X. 2015. Magnetic susceptibility application: a window onto ancient environments and climatic variations: foreword. Geological Society, London, Special Publications 414: 1–13.

Da Silva A-C., Yans J, Boulvain F. 2010. Sedimentology and magnetic susceptibility during the "punctata" event of the Ardenne area (Belgium): identification of severe and rapid sea level fluctuations, in: Magnetic Susceptibility, Correlations and Palaeozoic Environments, edited by A.-C. Da Silva and F. Boulvain pp. 319-322.

De Baar HJW, Brewer PG, Bacon MP. 1985. Anomalies in rare earth distributions in seawater: Gd and Tb. Geochim Cosmochim Acta 49: 1961–1969.

Dekkers MJ. 1989. Magnetic Properties of Natural Goethite—II. TRM behaviour during thermal and alternating field demagnetization and low-temperature treatment. Geophys J Int 97: 341–355.

Döebelin N, Kleeberg R. 2015. Profex: a graphical user interface for the Rietveld refinement program BGMN. J Appl Cryst 48: 1573–1580.

Dunlop DJ, Özdemir, Ö. (Eds.) 1997. Rock Magnetism: Fundamentals and Frontiers. Cambridge Studies in Magnetism.

El Bamiki R, Raji O, Ouabid M, Elghali A, Khadiri Yazami O, Bodinier J-L. 2021. Phosphate rocks: a review of sedimentary and igneous occurrences in Morocco. Minerals 11: 1137.

El Bamiki R, Séranne M, Chellaï EH, Merzeraud G, Marzoqi M, Melinte-Dobrinescu MC. 2020. The Moroccan High Atlas phosphate-rich sediments: unraveling the accumulation and differentiation processes. Sediment Geol 403: 105655.

El Bamiki R, Séranne M, Parat F, Aubineau J, Chellaï EH, Marzoqi M, Bodinier J-L. 2023. Post-phosphogenesis processes and the natural beneficiation of phosphates: geochemical evidence from the Moroccan High Atlas phosphate-rich sediments. Chem Geol 631: 121523.

Ellouz N, Patriat M, Gaulier, J.-M., Bouatmani R, Sabounji S. 2003. From rifting to Alpine inversion: Mesozoic and Cenozoic subsidence history of some Moroccan basins. Sediment Geol 156: 185–212.

Ellwood BB, Crick RE, El Hassani A. 1999. The Magneto-Susceptibility Event and Cyclostratigraphy (MSEC) Method Used in Geological Correlation of Devonian Rocks from Anti-Atlas Morocco1. AAPG Bull 83: 1119–1134.

Ellwood BB, Crick RE, Hassani AE, Benoist SL, Young RH. 2000. Magnetosusceptibility event and cyclostratigraphy method applied to marine rocks: detrital input versus carbonate productivity. Geology 28: 1135–1138.

Ellwood BB, El Hassani A, Tomkins JH, Bultynck P. 2015. A climate-driven model and development of a floating-point timescale for the middle devonian Eifelian stage using time-series analysis of magnetic susceptibility (x) data set, in: Magnetic Susceptibility Application – a Window onto Ancient Environments and Climatic Variations, edited by Da Silva AC, Whalen MT, Hladil J, Chadimova L, Chen D, Spassov S, Boulvain F, Devleeschouwer, X.

Fedo CM, Babechuk MG. 2022. Petrogenesis of siliciclastic sediments and sedimentary rocks explored in three-dimensional Al2O3-CaO*+Na2O-K2O-FeO+MgO (A-CN-K-FM) compositional space. Can J Earth Sci 60: 818–838.

Fedo CM, Wayne Nesbitt H, Young GM. 1995. Unraveling the effects of potassium metasomatism in sedimentary rocks and paleosols, with implications for paleoweathering conditions and provenance. Geology 23: 921–924.

Flinn D. 1978. Construction and computation of three-dimensional progressive deformations. J Geolog Soc 135: 291–305.

Font E, Carlut J, Rémazeilles C, Mather TA, Nédélec A, Mirão, J., Casale S. 2017. End-Cretaceous akaganéite as a mineral marker of Deccan volcanism in the sedimentary record. Sci Rep 7: 11453.

Font E, Fabre S, Nédélec A, Adatte T, Keller G, Viega-Pires C, Ponte J, Mirão, J., Khozyem H, Spangenberg JE. 2014. Atmospheric halogen and acid rains during the main phase of Deccan eruptions: magnetic and mineral evidence, in: Keller G, Kerr, A.C. (Eds.),

Volcanism, Impacts, and Mass Extinctions: Causes and Effects. Geological Society of America pp. 353-368.
Font E, Nédélec A, Ellwood BB, Mirão J, Silva PF. 2011. A new sedimentary benchmark for the Deccan Traps volcanism? Geophys Res Lett 38. https://doi.org/10.1029/2011GL049824
Frizon de Lamotte D, Zizi M, Missenard Y, Hafid M, El Azzouzi M, Maury RC, Charrière A, Taki Z, Benammi M, Michard A, 2008. The Atlas System, in: Michard, André, Saddiqi O, Chalouan A, Frizon de Lamotte, Dominique (Eds.), Continental Evolution: The Geology of Morocco: Structure, Stratigraphy, and Tectonics of the Africa-Atlantic-Mediterranean Triple Junction, Lecture Notes in Earth Sciences. Springer, Berlin, Heidelberg, pp. 133-202.
Frizon de Lamotte DF, Leturmy P, Missenard Y, Khomsi S, Ruiz G, Saddiqi O, Guillocheau F, Michard A. 2009. Mesozoic and Cenozoic vertical movements in the Atlas system (Algeria, Morocco, Tunisia): an overview. Tectonophysics 475: 9–28.
Gao Y, Ibarra DE, Caves Rugenstein JK, Chen J, Kukla T, Methner K, Gao Y, Huang H, Lin Z, Zhang L, Xi D, Wu H, Carroll AR, Graham SA, Chamberlain CP, Wang C. 2021. Terrestrial climate in mid-latitude East Asia from the latest Cretaceous to the earliest Paleogene: a multiproxy record from the Songliao Basin in northeastern China. Earth-Sci Rev 216: 103572.
Garnit H, Bouhlel S, Barca D, Chtara C. 2012. Application of LA-ICP-MS to sedimentary phosphatic particles from Tunisian phosphorite deposits: Insights from trace elements and REE into paleo-depositional environments. Geochemistry 72: 127–139.
Girard C, Feist R, Mossoni A, Cornée J-J., Camps P, Charruault A-L., Corradini C. 2021. North-Gondwana – Laurussia dynamic paleogeography challenged by magnetic susceptibility through the Famennian. Gondwana Res 97: 263–272.
Herbig H-G., Trappe J. 1994. Stratigraphy of the Subatlas Group (Maastrichtian – Middle Eocene, Morocco). Newsl Stratigr 125–165.
Hillier S. 2000. Accurate quantitative analysis of clay and other minerals in sandstones by XRD: comparison of a Rietveld and a reference intensity ratio (RIR) method and the importance of sample preparation. Clay Minerals 35: 291–302.
Hladil J. 2002. Geophysical records of dispersed weathering products on the Frasnian carbonate platform and early Famennian ramps in Moravia, Czech Republic: proxies for eustasy and palaeoclimate. Palaeogeogr Palaeoclimatol Palaeoecol 181: 213–250.
Jelinek V. 1981. Characterization of the magnetic fabric of rocks. Tectonophysics 79: T63– T67.
Jian X, Guan P, Zhang W, Feng F. 2013. Geochemistry of Mesozoic and Cenozoic sediments in the northern Qaidam basin, northeastern Tibetan Plateau: implications for provenance and weathering. Chem Geol 360-361: 74–88.
Johnston JH. 1977. Jarosite and akaganéite from White Island volcano, New Zealand: an X-ray and Mössbauer study. Geochim Cosmochim Acta 41: 539–544.
Knidiri A, Daoudi L, El Ouahabi M, Rhouta B, Rocha F, Fagel N. 2014. Palaeogeographic controls on palygorskite occurrence in Maastrichtian-Palaeogene sediments of the Western High Atlas and Meseta Basins (Morocco). Clay Minerals 49: 595–608.
Kocsis L, Gheerbrant E, Mouflih M, Cappetta H, Yans J, Amaghzaz M. 2014. Comprehensive stable isotope investigation of marine biogenic apatite from the late Cretaceous-early Eocene phosphate series of Morocco. Palaeogeogr Palaeoclimatol Palaeoecol 394: 74–88.
Kosterov A. 2002. Low-temperature magnetic hysteresis properties of partially oxidized magnetite. Geophys J Int 149: 796–804.
Lanari R, Fellin MG, Faccenna C, Balestrieri ML, Pazzaglia FJ, Youbi N, Maden C. 2020. Exhumation and surface evolution of the Western High Atlas and surrounding regions as constrained by low-temperature thermochronology. Tectonics 39: e2019T C005562.
Leprêtre R, Missenard Y, Barbarand J, Gautheron C, Jouvie I, Saddiqi O. 2018. Polyphased Inversions of an Intracontinental Rift: case study of the Marrakech High Atlas, Morocco. Tectonics 37: 818–841.
Li L, Keller G. 1998. Maastrichtian climate, productivity and faunal turnovers in planktic foraminifera in South Atlantic DSDP sites 525A and 21. Mar Micropaleontol 33: 55–86.
Lowrie W, Alvarez W, Asaro F. 1990. The origin of the White Beds below the Cretaceous-Tertiary boundary in the Gubbio section, Italy. Earth Planet Sci Lett 98: 303–312.
Mahboubi A, Cornée, J.-J., Feist R, Camps P, Girard C. 2019. Frasnian (Upper Devonian) integrated facies analysis, magnetic susceptibility and sea-level fluctuations in the NW Algerian Sahara. Geolog Mag 156: 1295–1310.
McClellan GH, Van Kauwenbergh SJ. 1991. Mineralogical and chemical variation of francolites with geological time. J Geolog Soc 148: 809–812.
Mead GA, Tauxe L, LaBrecque JL. 1986. Oligocene paleoceanography of the South Atlantic: Paleoclimatic implications of sediment accumulation rates and magnetic susceptibility measurements. Paleoceanography 1: 273–284.
Meunier A, Caner L, Hubert F, Albani AE, Prêt D. 2013. The weathering intensity scale (WIS): An alternative approach of the Chemical Index of Alteration (CIA). Am J Sci 313: 113–143.
Michard A, Saddiqi O, Chalouan A, Frizon de Lamotte D. 2008. Continental Evolution: The Geology of Morocco. Springer, Berlin, Heidelberg.
Missenard Y, Saddiqi O, Barbarand J, Leturmy P, Ruiz G, El Haimer F-Z., Frizon de Lamotte D. 2008. Cenozoic denudation in the Marrakech High Atlas, Morocco: insight from apatite fission-track thermochronology. Terra Nova 20: 221–228.
Morin FJ. 1950. Magnetic susceptibility of α Fe2 O3 and α Fe2 O3 with added titanium. Phys Rev 78: 819–820.
Nathan Y. 1984. The Mineralogy and Geochemistry of Phosphorites, in: Nriagu JO, Moore, P.B. (Eds.), Phosphate Minerals. Berlin, Heidelberg: Springer-Verlag, pp. 275-291.
Nesbitt HW, Young GM, 1982. Early Proterozoic climates and plate motions inferred from major element chemistry of lutites. Nature 299: 715–717.
Nguidi MA, Mouflih M, Benbouziane A, Kocsis L, El Ouariti S, El Boukhari H, Aquit M, Yazami OK. 2021. Lithofacies analysis, sedimentary dynamics and genesis of Maastrichtian-Eocene phosphorites of BouCraa deposit (Southern Morocco). J Afr Earth Sci 177: 104161.
Nowaczyk NR, Minyuk P, Melles M, Brigham-Grette J, Glushkova O, Nolan M, Lozhkin AV, Stetsenko TVM, Andersen P, Forman SL. 2002. Magnetostratigraphic results from impact crater Lake El'gygytgyn, northeastern Siberia: a 300 kyr long high-resolution terrestrial palaeoclimatic record from the Arctic. Geophys J Int 150: 109–126.
Özdemir Ö, Dunlop DJ. 2010. Hallmarks of maghemitization in low-temperature remanence cycling of partially oxidized magnetite nanoparticles. J Geophys Res: Solid Earth 115. https://doi.org/10.1029/2009JB006756
Özdemir Ö, Dunlop DJ. 2005. Thermoremanent magnetization of multidomain hematite. J Geophys Res: Solid Earth 110. https://doi.org/10.1029/2005JB003820

Özdemir Ö, Dunlop DJ, Moskowitz BM. 2002. Changes in remanence, coercivity and domain state at low temperature in magnetite. Earth Planet Sci Lett 194: 343–358.

Pas D, Da Silva A-C., Poulain G, Spassov S, Boulvain F. 2019. Magnetic Susceptibility Record in Paleozoic Succession (Rhenohercynian Massif, Northern Europe) – Disentangling Sea Level, Local and Diagenetic Impact on the Magnetic Records. Front Earth Sci 7.

Paterson GA, Zhao X, Jackson M, Heslop D. 2018. Measuring, processing, and analyzing hysteresis data. Geochem Geophys Geosyst 19: 1925–1945.

Potter DK, Stephenson A. 1988. Single-domain particles in rocks and magnetic fabric analysis. Geophys Res Lett 15: 1097–1100.

Pufahl PK, Groat LA. 2017. Sedimentary and igneous phosphate deposits: formation and exploration: an invited paper. Econ Geol 112: 483–516.

Reynard B, Lécuyer C, Grandjean P. 1999. Crystal-chemical controls on rare-earth element concentrations in fossil biogenic apatites and implications for paleoenvironmental reconstructions. Chem Geol 155: 233–241.

Riquier L, Averbuch O, Devleeschouwer X, Tribovillard N. 2010. Diagenetic versus detrital origin of the magnetic susceptibility variations in some carbonate Frasnian-Famennian boundary sections from Northern Africa and Western Europe: implications for paleoenvironmental reconstructions. Int J Earth Sci (Geol Rundsch) 99: 57–73.

Robinson SG. 1986. The late Pleistocene palaeoclimatic record of North Atlantic deep-sea sediments revealed by mineral-magnetic measurements. Phys Earth Planetary Interiors 42: 22–47.

Rohais S, Hamon Y, Deschamps R, Beaumont V, Gasparrini M, Pillot D, Romero-Sarmiento, M-F. 2019. Patterns of organic carbon enrichment in a lacustrine system across the K-T boundary: insight from a multi-proxy analysis of the Yacoraite Formation, Salta rift basin, Argentina. Int J Coal Geol 210: 103208.

Schneider J, Bechstädt T, Machel HG. 2004. Covariance of C- and O-isotopes with magnetic susceptibility as a result of burial diagenesis of sandstones and carbonates: an example from the Lower Devonian La Vid Group, Cantabrian Zone, NW Spain. Int J Earth Sci (Geol Rundsch) 93: 990–1007.

Schuffert JD, Kastner M, Emanuele G, Jahnke RA. 1990. Carbonate-ion substitution in francolite: a new equation. Geochim Cosmochim Acta 54: 2323–2328.

Schwertmann U, Cornell RM. 1991. Iron Oxides in the Laboratory: Preparation and Characterization. John Wiley & Sons.

Shields G, Stille P. 2001. Diagenetic constraints on the use of cerium anomalies as palaeoseawater redox proxies: an isotopic and REE study of Cambrian phosphorites. Chemical Geology, Response of the Oceanic / Atmospheric Systems to Past Global Changes 175: 29–48.

Singer A, Galan E. 1984. Palygorskite-Sepiolite: Occurrences, Genesis and Uses. Amsterdam: Elsevier.

Środoń J, Eberl DD. 1984. Illite, in: Review in Mineralogy Vol. 13, Micas, edited by S.W. Bailey. Mineralogical Society of America, Washington DC, pp. 495-544.

Stage M. 2001. Magnetic susceptibility as carrier of a climatic signal in chalk. Earth Planet Sci Lett 188: 17–27.

Tauxe L, Gee JS, Staudigel H. 1998. Flow directions in dikes from anisotropy of magnetic susceptibility data: the bootstrap way. J Geophys Res 103: 17775–17790.

Taylor SN, Lagroix F, Rousseau D-D., Antoine P. 2014. Mineral magnetic characterization of the Upper Pleniglacial Nussloch loess sequence (Germany): an insight into local environmental processes. Geophys J Int 199: 1463–1480.

Taylor SR, McLennan SM. 1985. The continental crust: Its composition and evolution. Blackwell Scientific Publications, Oxford.

Vanderaveroet P, Averbuch O, Deconinck J-F., Chamley H. 1999. A record of glacial/interglacial alternations in Pleistocene sediments off New Jersey expressed by clay mineral, grain-size and magnetic susceptibility data. Marine Geol 159: 79–92.

Velde B, Suzuki T, Nicot E. 1986. Pressure-temperature-composition of illite/smectite mixed-layer minerals: Niger delta mudstones and other examples. Clays Clay Minerals 34: 435–441.

Verwey E. 1935. The crystal structure of γ-Fe2O3 and γ-Al2 O3. Zeitsch Kristallogr Crystalline Mater. 91: 65–69.

Walker JCG, Hays PB, Kasting JF. 1981. A negative feedback mechanism for the long-term stabilization of Earth's surface temperature. J Geophys Res: Oceans 86: 9776–9782.

Walker RG, James NP. 1992. Facies Models: Response to Sea Level Change. Geological Association of Canada, Geotext. ed.

Warr LN. 2022. Earth's clay mineral inventory and its climate interaction: a quantitative assessment. Earth-Sci Rev 234: 104198.

Westerhold T, Marwan N, Drury AJ, Liebrand D, Agnini C, Anagnostou E, Barnet JSK, Bohaty SM, De Vleeschouwer D, Florindo F, Frederichs T, Hodell DA, Holbourn AE, Kroon D, Lauretano V, Littler K, Lourens LJ, Lyle M, Pälike H, Röhl U, Tian J, Wilkens RH, Wilson PA, Zachos JC. 2020. An astronomically dated record of Earth's climate and its predictability over the last 66 million years. Science 369: 1383–1387.

Whalen MT, Day JE. (Jed). 2010. Cross-Basin Variations in Magnetic Susceptibility Influenced by Changing Sea Level, Paleogeography, and Paleoclimate: Upper Devonian, Western Canada Sedimentary Basin. J Sedimentary Res 80: 1109–1127.

Wouters S, Spassov S, Martinez M, Steurbaut E, Storme J-Y., Yans J, Devleeschouwer X. 2019. Depositional changes during the Danian-Selandian transition in Loubieng (France), Zumaia (Spain) and Sidi Nasseur (Tunisia): insights from and limits of rock magnetism. Geolog Mag 156: 1982–2000.

Zhang R, Kravchinsky VA, Zhu R, Yue L. 2010. Paleomonsoon route reconstruction along a W-E transect in the Chinese Loess Plateau using the anisotropy of magnetic susceptibility: Summer monsoon model. Earth Planet Sci Lett 299: 436–446.

Cite this article as: Aubineau J, Antonio PYJ, El Bamiki R, Parat F, Camps P, Raji O, Jourani E-S, Bodinier J-L, Macouin M, Gilder S, Rousse S, Séranne M. 2024. Magnetic susceptibility controlled by climate-driven weathering intensity, *BSGF - Earth Sciences Bulletin* 195: 25.